The Zipped Finite Element Method: High-order shape functions for polygons

Computer Methods in Applied Mechanics and Engineering 458 (2026) 119060

Contents lists available at ScienceDirect

Comput. Methods Appl. Mech. Engrg.

journal homepage: www.elsevier.com/locate/cma

The Zipped Finite Element Method: High-order shape functions for polygons

Stefano Berrone [a,1], Lorenzo Neva [a,1], Moreno Pintore [b], Gioana Teora [a,*,1], Fabio Vicini [a,1]

[a] Dipartimento di Scienze Matematiche "G. L. Lagrange", Politecnico di Torino, Corso Duca degli Abruzzi 24, Torino, 10129, Italy
[b] Laboratoire Jacques-Louis Lions, Sorbonne Université, MEGAVOLT Team, Inria, 4 place Jussieu, Paris, 75005, France

ARTICLE INFO

Dataset link: https://github.com/AURION-Polito/Art-ZFEM-2D

Keywords:
Shape functions
High-order
Polygonal method
Star-shaped

ABSTRACT

In this paper, we present a new polygonal finite element method, called the Zipped Finite Element Method, for star-shaped polygons. The proposed approach constructs high-order shape functions as linear combinations of standard finite element basis functions defined on a local trivial sub-triangulation of each element. This refinement is used solely for the construction of the shape functions and does not affect the final number of degrees of freedom. The resulting finite element space includes polynomials of the desired order and preserves conformity across elements. Consequently, the method inherits the convergence properties of the finite element framework under suitable mesh assumptions. Numerical experiments confirm the expected rates of convergence.

1. Introduction

The simulation of physical phenomena plays a crucial role in many engineering applications, where the numerical solution of partial differential equations is often required. Among the available numerical techniques, the Finite Element Method (FEM) [1,2] is one of the most widely used, due to its solid theoretical foundations. However, standard FEM formulations are constrained by the requirements of domain discretization. In two-dimensional problems, such as those considered in this work, the mesh is typically restricted to triangular or convex quadrilateral elements.

Among the strategies proposed to expand the set of admissible elements are unfitted methods [3,4], IsoGeometric Analysis (IGA) [5–7], Scaled boundary Finite Element Methods (SBFEM) [8–11], and Unsymmetric Finite Element Method (UFEM) [12–14]. There also exist several discretizations employing polygonal elements, such as Discontinuous Galerkin (DG) [15,16], High-Hybrid Order methods (HHO) [17], and Virtual Element Methods (VEM) [18,19], that, however, resort to stabilization techniques for the evident complexity of defining shape functions over generic polygons.

Since the pioneering work of Wachspress [20], who first introduced the concept of constructing nodal shape functions on general polygonal domains that form a partition-of-unity and are polynomial-complete, numerous studies have sought to generalize this idea [21]. A non-exhaustive list of representative works, limited to low-order basis functions, includes Mean Value Coordinates (MVC) [22,23], Maximum Entropy coordinates (MAXENT) [24], Natural Neighbor-based coordinates [25–27], a formulation for convex polygons with interior nodes [28], Smoothed Finite Element Method (SFEM) [29–31], the Lightning Virtual Element

* Corresponding author.
E-mail addresses: stefano.berrone@polito.it (S. Berrone), lorenzo.neva@polito.it (L. Neva), moreno.pintore@sorbonne-universite.fr (M. Pintore), gioana.teora@polito.it (G. Teora), fabio.vicini@polito.it (F. Vicini).
[1] The authors are members of the INdAM-GNCS.

https://doi.org/10.1016/j.cma.2026.119060
Received 19 December 2025; Received in revised form 3 April 2026; Accepted 4 May 2026

Method (LVEM) [32], reduced basis Virtual Element Method (rbVEM) [33], and the Neural Approximated Virtual Element Method (NAVEM) [34,35]. Despite the evident complexity of defining high-order basis functions over generic polygons, possibly including hanging nodes, their superior accuracy and convergence properties have long motivated research efforts in this direction [36]. A non-exhaustive list includes: the Spectral Element Method (SEM) [37,38] on triangular/quadrilateral elements in 2D, or tetrahedral/hexahedral elements in 3D, Serendipity Finite Element Methods on convex elements [39,40], and transfinite elements over quadtree/octree decompositions [41–44]. We also highlight the existence of high-order methods on curved elements [45], of methods based on rational basis functions [20], and of the Natural Element Coordinates (NECs) [46], which allow to define high-order basis functions independently of the problem dimension by using the natural neighbor interpolation.

Building on these developments, the objective of this work is to design an algorithm that constructs globally continuous high-order shape functions, which are known in a closed-form, for meshes composed of general star-shaped elements. The method combines the accuracy of high-order polynomial approximation with the geometric capability of a polygonal discretization, handling convex and concave elements as well as elements with hanging nodes within a unified numerical framework.

The method introduced in this paper is called the Zipped Finite Element Method (Z-FEM). The key idea of Z-FEM is to define high-order local basis functions as weighted combinations of standard FEM shape functions defined on a simple sub-triangulation of each element of the tessellation. This sub-triangulation of the element is obtained by connecting the vertices of the polygon to a suitably chosen interior point located within the kernel of the element. The coefficients of the linear combinations are determined by solving a local optimization problem, which can be efficiently decomposed into smaller sub-problems thanks to its structure. Moreover, the local space is designed so that polynomials of degree up to the method order can be reproduced. This property is fundamental, as it allows the method to inherit the theoretical framework of the FEM, ensuring both well-posedness of the discrete problem and optimal a priori error estimates. The term zipped reflects the key design principle of this approach: the local FEM discrete space built over the sub-triangulation is "compressed", as a zip file, by linearly combining the FEM basis functions to obtain a smaller space with fewer number of degrees of freedom, while preserving the essential properties of C^0-conformity and polynomial consistency on general polygonal elements. This method derives from studies performed by the authors in [47] in the NAVEM framework.

To the best of our knowledge, several related works have explored ideas similar to those presented in this paper, but remain limited to low-order formulations. In [48], the authors introduce a method based on conforming shape functions constructed as weighted combinations of standard FEM shape functions defined over a fan of simplices forming the polyhedron. Their formulation, restricted to first-order accuracy, is applied to star-shaped polygons in nonlinear solid mechanics. A first-order formulation is also proposed in [49] and later extended to second order in [50], where the authors emphasize the challenges of generalizing such basis functions to higher-order cases.

The paper is structured as follows. Section 2 presents the model problem and the notation used in the manuscript. Section 3 details and analyzes the required properties for the shape functions. In Section 4 we provide a theoretical justification for the appropriate choice of degrees of freedom. The optimization problem is presented, along with the algorithm adopted for its resolution. In Section 5, we define the local discrete space, demonstrate its local unisolvence, and discuss the theoretical properties of the new proposed method. Section 6 is dedicated to numerical experiments, which show the effectiveness of the method. Conclusions are drawn in Section 7.

The implementation of the Z-FEM has been released within the PolyDiM library [51]. Moreover, the code reproducing the numerical experiments presented in this paper is publicly available at the GitHub repository github.com/Art-ZFEM-2D.

2. Notations and the model problem

Throughout the paper, the usual notation for Sobolev spaces is adopted. Let $\omega \subset \mathbb{R}^2$ be a generic bounded domain, that can be a polygonal element E or the PDE domain Ω. Given two scalar functions $f, g \in L^2(\omega)$ and two vector fields $\mathbf{s}, \mathbf{t} \in \left[L^2(\omega)\right]^2$, we denote by $(f,g)_\omega$ and $(\mathbf{s},\mathbf{t})_\omega$ the two bilinear forms

$$(f,g)_\omega := \int_\omega fg, \qquad (\mathbf{s},\mathbf{t})_\omega := \int_\omega \mathbf{s}\cdot\mathbf{t}.$$

Furthermore, for any $s \geq 0$, $\|\cdot\|_{H^s(\omega)}$ and $|\cdot|_{H^s(\omega)}$ denote the norm and seminorm of functions in $H^s(\omega)$, respectively. By definition, $H^0(\omega) \equiv L^2(\omega)$. Lastly, the notation $\|\cdot\|_2$ denotes the standard Euclidean norm on $\mathbb{R}^2$.

Given a generic polygon E, let us introduce the space $\mathbb{P}_k(E)$ of two-dimensional polynomials of degree up to $k \in \mathbb{N}$ on E, whose dimension is $n_k := \frac{(k+1)(k+2)}{2}$. We adopt the standard convention $\mathbb{P}_{-m}(E) = \emptyset$ and $n_{-m} = 0$ for all $m \in \mathbb{N}$.

Let $\Omega \subset \mathbb{R}^2$ be a bounded convex domain with Lipschitz boundary $\partial\Omega$. We consider the following scalar diffusion-reaction problem with homogeneous Dirichlet boundary conditions:

$$\begin{cases} -\nabla\cdot(\boldsymbol{\kappa}\nabla u) + \gamma u = f & \text{in } \Omega, \\ u = 0 & \text{on } \Gamma = \partial\Omega, \end{cases} \tag{1}$$

where $\boldsymbol{\kappa} \in [L^\infty(\Omega)]^{2\times 2}$ is a diffusion tensor, uniformly symmetric positive definite over Ω, i.e. there exist two constants $0 < \alpha_1 \leq \alpha_2$ such that

$$\alpha_1\|\boldsymbol{\epsilon}\|_2 \leq \boldsymbol{\epsilon}^T\boldsymbol{\kappa}(\boldsymbol{x})\boldsymbol{\epsilon} \leq \alpha_2\|\boldsymbol{\epsilon}\|_2 \qquad \forall \boldsymbol{x} \in \Omega, \quad \forall \boldsymbol{\epsilon} \in \mathbb{R}^2. \tag{2}$$

Moreover, $\gamma \in L^\infty(\Omega)$, $\gamma(\boldsymbol{x}) \geq 0$ for all $\boldsymbol{x} \in \Omega$, is a reaction coefficient, and $f \in L^2(\Omega)$ is a scalar loading term.

The variational formulation of problem (1) reads as: *Find* $u \in \mathcal{V} := H^1_0(\Omega)$ *such that*

$$\mathcal{B}(u, v) = (f, v)_\Omega \quad \forall v \in \mathcal{V}, \tag{3}$$

where $\mathcal{B} : \mathcal{V} \times \mathcal{V} \to \mathbb{R}$ is the following symmetric, continuous, and coercive bilinear form

$$\mathcal{B}(u, v) := (\boldsymbol{\kappa} \nabla u, \nabla v)_\Omega + (\gamma u, v)_\Omega \quad \forall u, v \in \mathcal{V}. \tag{4}$$

Thanks to the Lax–Milgram Theorem [52], problem (3) admits a unique solution.

3. The zipped finite element space

Let Ω_h be a discretization of the domain Ω into non-overlapping polygonal elements E. The symbols N_v^E, $\mathcal{E}_{h,E}$, and h_E denote the number of vertices, the set of edges, and the diameter of the element E, respectively. In particular, the diameter of the element is defined as $h_E = \max_{\boldsymbol{x},\boldsymbol{y} \in E} \|\boldsymbol{x} - \boldsymbol{y}\|_2$. Moreover we set $h := \max_{E \in \Omega_h} h_E$.

We assume Ω_h to satisfy the following mesh assumptions.

Assumption 1 (*Mesh Assumptions*)**.** There exists a positive real number $\rho \in (0, 1)$, independent of h, such that

- for each element $E \in \Omega_h$ and each edge $e \in \mathcal{E}_{h,E}$, it holds $|e| \geq \rho h_E$;
- each element $E \in \Omega_h$ is star-shaped with respect to a ball of radius $\geq \rho h_E$.

Given an integer number $k \geq 1$, we define a finite-dimensional space $\mathcal{V}_{h,k} \subset \mathcal{V}$ as

$$\mathcal{V}_{h,k} := \{v \in C^0(\overline{\Omega}) \cap \mathcal{V} : \ v_{|E} \in \mathcal{V}_k(E) \ \forall E \in \Omega_h\} \quad \text{with} \quad N_{\text{dof}} := \dim \mathcal{V}_{h,k}, \tag{5}$$

where the elemental space $\mathcal{V}_k(E)$ can be described as

$$\mathcal{V}_k(E) := \text{span}\{\varphi_i^E : i = 1, \dots, N_{\text{dof}}^E\} \quad \text{with} \quad N_{\text{dof}}^E := \dim \mathcal{V}_k(E), \tag{6}$$

for a given set of local basis functions $\{\varphi_i^E\}_{i=1}^{N_{\text{dof}}^E}$. We aim to define the shapes of these basis functions and their number N_{dof}^E so that the following properties hold:

P.1 The set $\mathcal{V}_k(E)$ contains the set of polynomials $\mathbb{P}_k(E)$.

P.2 The elemental shape functions satisfy the Kronecker-Delta property with respect to a set of linearly independent linear operators

$$\text{dof}_i^E : \mathcal{V}_k(E) \to \mathbb{R} \qquad i = 1, \dots, N_{\text{dof}}^E, \tag{7}$$

termed Degrees of Freedom (DOFs in short), i.e. $\text{dof}_i^E(\varphi_j^E) = \delta_{ij}$ for all $i, j = 1, \dots, N_{\text{dof}}^E$.

P.3 The global counterparts of these basis functions are continuous across adjacent elements in Ω_h.

For this purpose, the first issue concerns the choice of the number of degrees of freedom that enable us to satisfy Properties **P.1** and **P.3**, regardless of the shape of the polygon. This problem has been extensively investigated in the framework of Serendipity element methods [40,53]. The number of degrees of freedom N_{dof}^E must be at least n_k, to include all polynomials of order $\leq k$ and satisfy Property **P.1**. Moreover, a degree of freedom for each vertex and $(k-1)$ degrees of freedom for each edge must be placed to guarantee Property **P.3**, resulting in a total number of $N_v^E k$ degrees of freedom on the boundary ∂E of the element E. In particular, if $k \leq 2$, these boundary degrees of freedom are sufficient to ensure both conformity and the unique identification of polynomials, since $N_v^E \geq 3$. When $k \geq 3$, instead, the minimum number of degrees of freedom required to satisfy Properties **P.1** and **P.3** for a convex polygon E is given by [40,53]

$$N_v^E k + n_{(k-\eta_E)},$$

where η_E denotes the number of straight lines needed to cover the entire boundary ∂E. For stability reasons, however, it is also important to determine the number η_E such that consecutive edges lying *almost* on the same straight lines are counted as one, while carefully defining what "almost" means. To avoid the stability and geometric issues arising from this ambiguity, while being able to handle convex, concave, and hanging-node elements indistinctly, we adopt the so-called *Serendipity lazy choice* [53], which consists of always including n_{k-3} internal degrees of freedom, that are sufficient to guarantee both stability and geometric independence.

Thus, the final number of local degrees of freedom is

$$N_{\text{dof}}^E = N_v^E k + n_{k-3}. \tag{8}$$

Consequently, the number of degrees of freedom depends solely on the number of vertices (and edges) of the element $E \in \Omega_h$ and on the order of accuracy k of the method. More specifically, on each edge e of E, we retain exactly $k+1$ degrees of freedom, i.e. the minimum number that allows to uniquely determine a polynomial of degree k on that edge, to ensure continuity and polynomial reproducibility. Moreover, for $k \geq 3$, we add n_{k-3} internal degrees of freedom to be able to reproduce two-dimensional polynomials in E. In the following section, we are going to define the nodal positions of these N_{dof}^E degrees of freedom and the related Lagrange basis functions $\{\varphi_i^E\}_{i=1}^{N_{\text{dof}}^E}$.

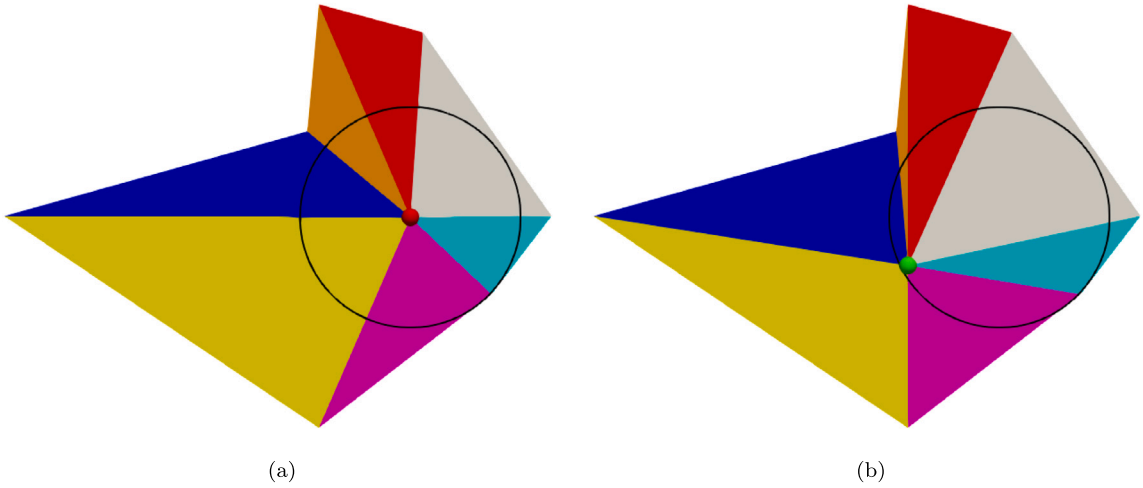

Fig. 1. Different sub-triangulations of a heptagon. Left: Sub-triangulation obtained by defining $\boldsymbol{x}^E$ (the red dot) as the solution of (10). Right: Sub-triangulation obtained by defining $\boldsymbol{x}^E$ (the green dot) as the solution of (11). The black line denotes the boundary of the greatest disk with respect to which the heptagon is star-shaped.

4. High-order shape functions on polygons

Let us consider a star-shaped polygon $E \subset \mathbb{R}^2$. Our aim is to determine a set of N^E_{dof} shape functions $\{\varphi^E_i\}_{i=1}^{N^E_{\text{dof}}}$ on E for a generic order $k \geq 1$ such that they satisfy Properties **P.1**, **P.2**, and **P.3**.

For this purpose, we adopt a similar approach to that proposed by [49] for the lowest order $k = 1$, while extending it to a generic order $k \geq 1$. Specifically, we compute these shape functions as a weighted combination of finite element shape functions living on a sub-triangulation of the element E, which can be trivially built under the assumption that E is star-shaped. Indeed, given an internal point $\boldsymbol{x}^E$ of the kernel of E, we can build a sub-triangulation $\mathcal{T}_E = \{T^E_j\}_{j=1}^{N^E_v}$ of E by connecting the N^E_v vertices $\{\boldsymbol{v}^E_j\}_{j=1}^{N^E_v}$ of E with $\boldsymbol{x}^E$ to form the following triangles:

$$T^E_j = \{\boldsymbol{x}^E, \boldsymbol{v}^E_j, \boldsymbol{v}^E_{j+1}\} \quad \forall j = 1, \dots, N^E_v, \tag{9}$$

where the symbol $\boldsymbol{v}^E_{N^E_v+1}$ denotes the vertex $\boldsymbol{v}^E_1$.

In particular, we define $\boldsymbol{x}^E$ and r^E as the center and the radius of the largest disk included in the kernel of E. Such quantities can be found as the solution of the following linear programming problem [54]:

$$\begin{aligned} \max_{(\boldsymbol{x}^E, r^E) \in \mathbb{R}^3} \quad & r^E \\ \text{such that} \quad & \boldsymbol{n}_e \cdot \boldsymbol{x}^E + r^E \leq b_e \quad \forall e \in \mathcal{E}_{h,E}, \\ & 0 < r^E \leq h_E, \end{aligned} \tag{10}$$

where, for each edge $e \in \mathcal{E}_{h,E}$, $\boldsymbol{n}_e$ denotes the unit outward normal vector to the edge e, and the scalar coefficient b_e is chosen in such a way that the edge lies on the line defined by the equation $\boldsymbol{n}_e \cdot \boldsymbol{x} = b_e$ for all $\boldsymbol{x} \in e$.

Remark 1. Another possible choice for $\boldsymbol{x}^E$ is the one described in [49], which yields highly accurate results in the linear case. Specifically, in such a paper, the internal point is determined as a weighted combination of the element vertices, i.e. $\boldsymbol{x}^E := \sum_{j=1}^{N^E_v} a^E_j \boldsymbol{v}^E_j$, where the weights are the least-norm solution of the following optimization problem:

$$\begin{aligned} \min_{\{a_j\}_{j=1}^{N^E_v}} \quad & \sum_{j=1}^{N^E_v} \text{area}(T^E_j)^2 \\ \text{such that} \quad & \sum_{j=1}^{N^E_v} a^E_j = 1. \end{aligned} \tag{11}$$

Here, instead, we adopt the alternative choice determined by (10) because it guarantees that the resulting global triangulation $\bigcup_{E \in \Omega_h} \mathcal{T}_E$ is shape-regular [55]. This property allows us to establish optimal error estimates (see Section 5). Nonetheless, numerical experiments do not reveal any significant difference in accuracy when using the various choices for $\boldsymbol{x}^E$. In Fig. 1, we illustrate the sub-triangulations obtained by defining $\boldsymbol{x}^E$ as the solution of (11) and (10) for a heptagon.

4.1. Standard basis functions over the element sub-triangulation

The standard finite element space of order $k \geq 1$ over the sub-triangulation $\mathcal{T}_E$ is defined as

$$\mathbb{V}_k(E;\mathcal{T}_E) := \{v \in C^0(\overline{E}) \cap H^1(E) : v_{|T} \in \mathbb{P}_k(T) \quad \forall T \in \mathcal{T}_E\}. \tag{12}$$

We observe that $\mathbb{P}_k(E) \subset \mathbb{V}_k(E;\mathcal{T}_E)$. Moreover, the dimension of this space is given by

$$N^E_{\Psi,k} := \left[(2k-1) + n_{k-3}\right] N^E_v + 1.$$

Let us introduce the finite element shape functions $\{\widehat{\Psi}^{\widehat{T}}_\ell\}_{\ell=1}^{n_k}$ over the reference triangle $\widehat{T} = \{(0,0),(1,0),(0,1)\}$. Let us consider the vector-valued function $\mathbf{pos} : \{1,\dots,n_k\} \to \mathbb{N}^3$ defined as

$$\mathbf{pos}(1) = (0,0,k), \quad \mathbf{pos}(2) = (1,0,k-1), \quad \dots, \quad \mathbf{pos}(k+1) = (k,0,0),$$
$$\mathbf{pos}(k+2) = (0,1,k-1), \quad \mathbf{pos}(k+3) = (1,1,k-2), \quad \dots, \quad \mathbf{pos}(2k+1) = (k-1,1,0), \quad \dots.$$

We introduce the following set of nodal coordinates in $\widehat{T}$, which are evenly distributed in each dimension, i.e.

$$\widehat{\boldsymbol{\xi}}_\ell := \frac{1}{k}\left(\mathbf{pos}_1(\ell), \mathbf{pos}_2(\ell)\right), \quad \text{for } \ell = 1,\dots,n_k,$$

where $\mathbf{pos}_d(\cdot)$, with $d = 1,2,3$, denotes the dth component of the vector $\mathbf{pos}(\cdot)$.

The finite element shape functions $\{\widehat{\Psi}^{\widehat{T}}_\ell\}_{\ell=1}^{n_k}$ defined with respect to this set of nodes are given by

$$\widehat{\Psi}^{\widehat{T}}_\ell(\widehat{\boldsymbol{x}}) = \prod_{d=1}^{3} \prod_{m=0}^{\mathbf{pos}_d(\ell)-1} \frac{\lambda_d(\widehat{\boldsymbol{x}}) - \frac{m}{k}}{\lambda_d(\widehat{\boldsymbol{\xi}}_\ell) - \frac{m}{k}} \qquad \forall\, \widehat{\boldsymbol{x}} := (\widehat{x}_1, \widehat{x}_2) \in \mathbb{R}^2,$$

where λ_d represent the barycentric coordinates related to the reference element, i.e.

$$\lambda_d(\widehat{\boldsymbol{x}}) = \widehat{x}_d \quad d = 1,2 \quad \text{and} \quad \lambda_3(\widehat{\boldsymbol{x}}) = 1 - \sum_{d=1}^{2} \widehat{x}_d.$$

We properly map these finite element functions to the sub-triangles $\{T^E_j\}_{j=1}^{N^E_v}$, and we glue them together to obtain a set of basis functions $\{\Psi^{\mathcal{T}_E}_n\}_{n=1}^{N^E_{\Psi,k}}$ for $\mathbb{V}_k(E;\mathcal{T}_E)$ that satisfy the Kronecker-Delta property with respect to the full set of nodes $\{\boldsymbol{\xi}^E_n\}_{n=1}^{N^E_{\Psi,k}} \in \overline{E}$, i.e.

$$\Psi^{\mathcal{T}_E}_m(\boldsymbol{\xi}^E_n) = \delta_{nm} \quad \forall n,m \in \mathcal{F}^E := \{1,\dots,N^E_{\Psi,k}\}. \tag{13}$$

4.2. Selection of the nodal coordinates

We observe that this set of functions satisfies Properties **P.1**, **P.2**, and **P.3**. Nevertheless, to reduce the dimension of the final space $\mathcal{V}_k(E)$, we select a subset $\mathcal{C}^E \subset \mathcal{F}^E$ of N^E_{dof} nodes $\{\boldsymbol{x}^E_i\}_{i\in\mathcal{C}^E}$ that allows us to satisfy these properties, while satisfying

$$n_k \leq N^E_{\text{dof}} \ll N^E_{\Psi,k}. \tag{14}$$

Here, N^E_{dof} is defined as in Eq. (8). Moreover, let us denote by $\mathcal{K}^E := \mathcal{F}^E \setminus \mathcal{C}^E$ the set of remaining indices, associated with the nodes $\{\boldsymbol{p}^E_j\}_{j\in\mathcal{K}^E}$, such that $\{\boldsymbol{p}^E_j\}_{j\in\mathcal{K}^E} \cup \{\boldsymbol{x}^E_i\}_{i\in\mathcal{C}^E} = \{\boldsymbol{\xi}^E_n\}_{n\in\mathcal{F}^E}$ and $\{\boldsymbol{p}^E_j\}_{j\in\mathcal{K}^E} \cap \{\boldsymbol{x}^E_i\}_{i\in\mathcal{C}^E} = \emptyset$, whose cardinality is

$$N^E_{\mathcal{K}} = N^E_{\Psi,k} - N^E_{\text{dof}}.$$

In the following, we will name the sets $\{\boldsymbol{\xi}^E_n\}_{n\in\mathcal{F}^E}$, $\{\boldsymbol{x}^E_i\}_{i\in\mathcal{C}^E}$, and $\{\boldsymbol{p}^E_j\}_{j\in\mathcal{K}^E}$ as the set of fine, coarse, and virtual nodes, respectively. Moreover, without loss of generality, we always assume that $\mathcal{C}^E = \{1,\dots,N^E_{\text{dof}}\}$ and, as a consequence, $\mathcal{K}^E = \{N^E_{\text{dof}}+1,\dots,N^E_{\Psi,k}\}$ to simplify notations.

Given this set of coarse nodes $\{\boldsymbol{x}^E_i\}_{i\in\mathcal{C}^E}$, we define the degrees of freedom introduced in Eq. (7) as

$$\text{dof}^E_i(v) := v(\boldsymbol{x}^E_i) \quad \forall i \in \mathcal{C}^E \quad \text{and} \quad \forall v \in \mathcal{V}_k(E). \tag{15}$$

Thus, the coarse nodes represent the nodal coordinates of the Z-FEM degrees of freedom. The set of coarse nodes with respect to which we define these linear operators must include all $N^E_v k$ degrees of freedom located on the boundary ∂E to ensure Property **P.3**. In addition, n_{k-3} DOFs internal to E must also be included (see the definition of N^E_{dof} in (8)). A strategy to properly select such internal nodal coordinates to guarantee polynomial reproducibility may be based on the following well-established theorem.

Theorem 1 (*Theorem 6.1 in [56]*). *Suppose $\{L_0,\dots,L_k\}$ are $k+1$ distinct lines on $\mathbb{R}^2$ and $U = \{\boldsymbol{x}_1,\dots,\boldsymbol{x}_{n_k}\}$ is a set of n_k distinct points such that $\boldsymbol{x}_1 \in L_0$, $\boldsymbol{x}_2, \boldsymbol{x}_3 \in L_1 \setminus L_0$, …, and $\boldsymbol{x}_{n_k-k},\dots,\boldsymbol{x}_{n_k} \in L_k \setminus \{L_0,\dots,L_{k-1}\}$. Then, there exists a unique polynomial of degree $\leq k$ that interpolates on U. Moreover, if $X = \{\boldsymbol{x}_1,\dots,\boldsymbol{x}_K\}$ with $U \subset X$, then X is k-unisolvent, i.e., the values of any polynomial of degree $\leq k$ at the points of X uniquely determine the polynomial itself.*

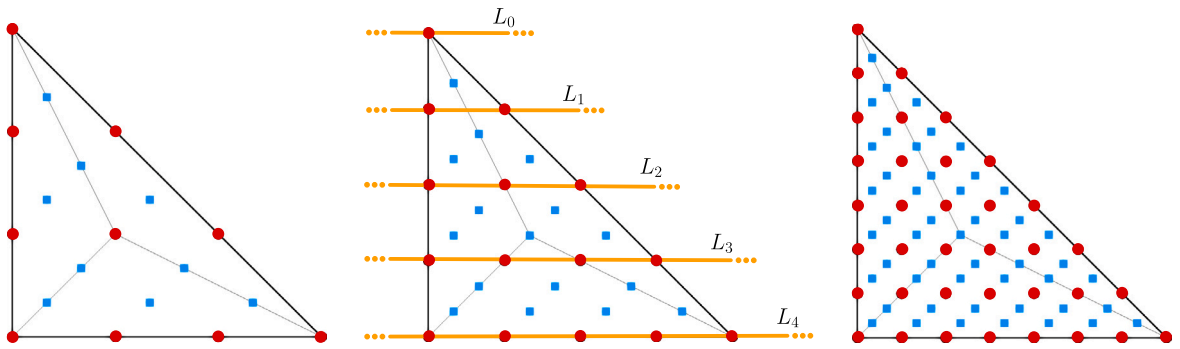

(a) $k = 3$. (b) $k = 4$. (c) $k = 7$.

Fig. 2. Selection of local N^E_{dof} DOFs on a triangular element E for different orders k. Red dots indicate $\mathcal{C}^E$, while blue squares represent $\mathcal{K}^E$. The yellow lines on $k = 4$ represent the distinct lines $\{L_0, \dots, L_k\}$ defined in Theorem 1.

Table 1
Number of internal degrees of freedom selected for each triangle inside a concave pentagon P and a concave octagon O according to our heuristic strategy. Vertical lines separate triangle groups. For example, for $k = 4$ and for the element O, we separate triangles into two groups: $\{T_1^O, T_2^O, T_3^O, T_4^O\}$ and $\{T_5^O, T_6^O, T_7^O, T_8^O\}$ that are divided in the table by a vertical line.

k	$n_{k-3}-1$	T_1^P	T_2^P	T_3^P	T_4^P	T_5^P	T_1^O	T_2^O	T_3^O	T_4^O	T_5^O	T_6^O	T_7^O	T_8^O
4	2	1	0	0	1	0	1	0	0	0	1	0	0	0
5	5	1	1	1	1	1	1	1	1	0	1	0	1	0
6	9	2	2	2	2	1	2	1	1	1	1	1	1	1
7	14	3	3	3	3	2	2	2	2	2	2	2	1	1

From this theorem, one can establish a rigorous criterion for selecting at least n_{k-3} internal points among the available degrees of freedom to ensure the inclusion of the required polynomials.

In particular, we observe that the standard Finite Element Method on triangular meshes can be derived from our method by using the rule provided by Theorem 1 for the selection of the coarse nodes. To illustrate this, Fig. 2 shows the set of fine nodes on the reference triangle for orders $k \in \{3, 4, 7\}$, highlighting the choice for the coarse nodes for which the Z-FEM space coincides exactly with the standard Lagrange FEM space. For $k > 2$, the selected points are located along the equispaced lines $\{L_0, \dots, L_k\}$ parallel to one of the edges of the E, which are drawn for the case $k = 4$ in Fig. 2(b). We remark that this choice satisfies Theorem 1, while allowing the Z-FEM formulation to coincide exactly with the classical Lagrange finite element on triangular elements.

However, when more intricate geometries are handled, such as concave elements or elements having hanging nodes, selecting internal points that rigorously satisfy Theorem 1 becomes geometrically complex and computationally demanding. For these reasons, we propose an alternative strategy for the selection of internal points aimed at reducing the local computational cost. In the numerical tests, this strategy is applied to all polygons independently of their geometry and leads to satisfactory results in each tested case.

The proposed selection strategy is guided by two main principles:

- minimizing internal point alignment;
- ensuring a homogeneous spatial distribution of internal points within the polygon.

To this end, a heuristic reordering algorithm is implemented. For any $k \geq 3$, for simplicity, we always select the nodal coordinates corresponding to $\boldsymbol{x}^E$ among the coarse nodes. Thus, for $k \geq 4$, we have to select the remaining $n_{k-3}-1$ internal coarse nodes. Starting from the natural vertex ordering, the triangles are divided into $n_{k-3} - 1$ groups and then interleaved following a regular pattern determined by the ratio between the total number of triangles and the number of groups. This procedure yields a spatially balanced indexing that provides uniform coverage of the domain and prevents local clustering of points. The same reordering pattern is then applied to determine the sequence of internal point selection within each triangle, further reducing local alignment and improving geometric uniformity. The subdivision of the triangles into groups and the corresponding assignment of the DOFs to each triangle in the case of a concave pentagon and a convex octagon are shown in Table 1 for $k \in \{4, 5, 6, 7\}$, while the corresponding selected nodal coordinates are shown in Fig. 3 for $k \in \{4, 6\}$.

We observe that the proposed algorithm does not formally guarantee that the selected points satisfy Theorem 1. To address this issue, one can always perform a local test like the one presented in Section 6.1, or equivalently, the test described in Remark 2, to assess the extent to which polynomials are included in the local space. If the results are not satisfactory, the number of promoted degrees of freedom can be increased to ensure that all required polynomials are included. In the limit, our method coincides with a standard Lagrange Finite Element Method on the triangulation $\bigcup_{E\in\Omega_h} \mathcal{T}_E$. The numerical experiments show that the proposed heuristic procedure consistently achieves high accuracy with the prescribed initial number of degrees of freedom stated in (8).

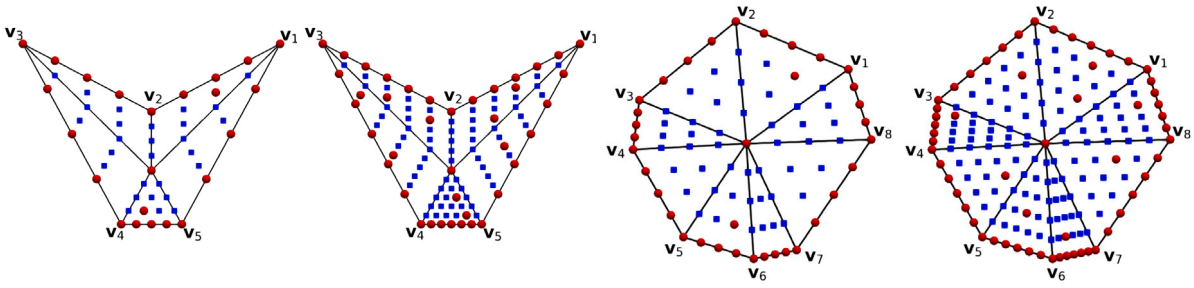

(a) $k = 4$. (b) $k = 6$. (c) $k = 4$. (d) $k = 6$.

Fig. 3. Selection of local N^E_{dof} DOFs with the proposed heuristic procedure on a concave pentagon and a convex octagon. Red dots indicate $\mathcal{C}^E$, while blue squares represent $\boldsymbol{\mathcal{K}}^E$.

4.3. The Z-FEM shape functions

Given a set of fine nodes, divided into coarse and virtual nodes, we can write new shape functions for the polygon E as a weighted combination of finite element basis functions on $\mathcal{T}_E$. More precisely, we write the final shape functions as

$$\varphi_i^E(\boldsymbol{x}) = \Psi_i^{\mathcal{T}_E}(\boldsymbol{x}) + \sum_{j \in \boldsymbol{\mathcal{K}}^E} \omega_{ij}^E \Psi_j^{\mathcal{T}_E}(\boldsymbol{x}) \quad \forall i = 1, \dots, N^E_{\text{dof}}, \quad \forall \boldsymbol{x} \in \overline{E}, \tag{16}$$

for a given set of weights $\omega_{ij}^E \in \mathbb{R}$, for all $i \in \mathcal{C}^E$ and $j \in \boldsymbol{\mathcal{K}}^E$. Now, we show how to determine these weights to satisfy Property **P.1**, i.e. to guarantee polynomial reproducibility.

Let us introduce the set of two-dimensional (scaled) monomials of degree up to k on a polygon E:

$$\mathcal{M}_k(E) = \left\{ m_\alpha(\boldsymbol{x}) = \left(\frac{\boldsymbol{x} - \boldsymbol{x}^E}{h_E} \right)^{\boldsymbol{\alpha}} : \boldsymbol{\alpha} = \mathbf{idx}(\alpha) \ \ \forall \alpha = 1, \dots, n_k \right\}, \tag{17}$$

where $\mathbf{idx} : \{1, \dots, n_k\} \to \mathbb{N}^2$ is defined as

$$\mathbf{idx}(1) = (0,0), \quad \mathbf{idx}(2) = (1,0), \quad \mathbf{idx}(3) = (0,1), \quad \mathbf{idx}(4) = (2,0), \quad \dots. \tag{18}$$

Given the set $\{\varphi_i^E\}_{i=1}^{N^E_{\text{dof}}}$ of basis functions of $\mathcal{V}_k(E)$, if a polynomial $p \in \mathbb{P}_k(E)$ belongs to $\mathcal{V}_k(E)$ then it can be expressed as

$$p(\boldsymbol{x}) = \sum_{i=1}^{N^E_{\text{dof}}} \text{dof}_i^E(p) \varphi_i^E(\boldsymbol{x}) \quad \forall \boldsymbol{x} \in \overline{E}. \tag{19}$$

Therefore, to ensure that $p \in \mathcal{V}_k(E)$ for any $p \in \mathbb{P}_k(E)$, we can choose the weights ω_{ij}^E such that the following equations are satisfied for each $\alpha = 1, \dots, n_k$ and each virtual node $\boldsymbol{p}_n^E$, with $n \in \boldsymbol{\mathcal{K}}^E$:

$$\begin{aligned} m_\alpha(\boldsymbol{p}_n) &= \sum_{i=1}^{N^E_{\text{dof}}} \text{dof}_i^E(m_\alpha) \varphi_i^E(\boldsymbol{p}_n^E) \\ &= \sum_{i=1}^{N^E_{\text{dof}}} \text{dof}_i^E(m_\alpha) [\Psi_i^{\mathcal{T}_E}(\boldsymbol{p}_n^E) + \sum_{j \in \boldsymbol{\mathcal{K}}^E} \omega_{ij} \Psi_j^{\mathcal{T}_E}(\boldsymbol{p}_n^E)] \\ &= \sum_{i=1}^{N^E_{\text{dof}}} \text{dof}_i^E(m_\alpha) \omega_{in}, \end{aligned} \tag{20}$$

where the last result derives once more from the Kronecker-Delta property of the finite element basis functions with respect to the fine nodes.

Let us introduce the matrices $\mathbf{D} \in \mathbb{R}^{n_k \times N^E_{\text{dof}}}$, $\mathbf{V} \in \mathbb{R}^{n_k \times N^E_{\boldsymbol{\mathcal{K}}}}$, and $\mathbf{W} \in \mathbb{R}^{N^E_{\text{dof}} \times N^E_{\boldsymbol{\mathcal{K}}}}$, whose entries are defined as

$$\begin{aligned} &\mathbf{D}(\alpha, i) := \text{dof}_i^E(m_\alpha) = m_\alpha(\boldsymbol{x}_i^E) \quad \forall \alpha = 1, \dots, n_k, \quad \forall i = 1, \dots, N^E_{\text{dof}}, \\ &\mathbf{V}(\alpha, j - N^E_{\text{dof}}) := m_\alpha(\boldsymbol{p}_j^E) \quad \forall \alpha = 1, \dots, n_k, \quad \forall j = N^E_{\text{dof}} + 1, \dots, N^E_{\Psi,k}, \\ &\mathbf{W}(i, j - N^E_{\text{dof}}) := \omega_{ij} \quad \forall i = 1, \dots, N^E_{\text{dof}}, \quad \forall j = N^E_{\text{dof}} + 1, \dots, N^E_{\Psi,k}. \end{aligned}$$

The constraint (20) can be equivalently rewritten as

$$\mathbf{DW}(:, n) = \mathbf{V}(:, n) \quad \forall n = 1, \dots, N^E_{\boldsymbol{\mathcal{K}}}, \tag{21}$$

where $\mathbf{W}(:, n)$ and $\mathbf{V}(:, n)$ denote the nth column of $\mathbf{W}$ and $\mathbf{V}$, respectively.

If $N^E_{\text{dof}} = n_k$, then $\mathbf{D}$ is a square non-singular matrix and the system of Eqs. (21) admits a unique solution gathered in the matrix $\mathbf{W}$ for any choice of coarse nodes that satisfies Theorem 1. However, when $N^E_v > 3$, the local number of degrees of freedom N^E_{dof} exceeds n_k in order to satisfy the conformity requirements stated in **P.3**. Consequently, the problem (21) is typically underdetermined. To overcome this issue, we determine the weights by solving the following minimization problem:

$$\min_{\mathbf{W}\in\mathbb{R}^{N^E_{\text{dof}}\times N^E_{\mathcal{K}}}} \sum_{i\in\mathcal{C}^E}\sum_{j\in\mathcal{K}^E} (\omega^E_{ij})^2 \tag{22}$$

$$\text{such that} \quad \mathbf{D}\mathbf{W} = \mathbf{V}. \tag{23}$$

We observe that the choice of minimizing the sum of the squared weights reflects the intent to promote a uniform contribution of all the virtual functions in determining the coarse functions [49].

To solve the minimization problem (22)–(23), we can solve the corresponding Karush-Kuhn–Tucker (KKT) system:

$$\begin{bmatrix} \mathbf{Q} & \mathbf{A}^T \\ \mathbf{A} & \mathbf{O} \end{bmatrix} \begin{bmatrix} \boldsymbol{\omega} \\ \lambda \end{bmatrix} = \begin{bmatrix} \mathbf{0} \\ \boldsymbol{b} \end{bmatrix}, \tag{24}$$

where

$$\begin{aligned} \mathbf{Q} &= 2\,\mathbf{I} \in \mathbb{R}^{N^E_{\text{dof}}N^E_{\mathcal{K}}\times N^E_{\text{dof}}N^E_{\mathcal{K}}}, \\ \mathbf{A} \in \mathbb{R}^{n_k N^E_{\mathcal{K}}\times N^E_{\text{dof}}N^E_{\mathcal{K}}} &: \mathbf{A} = \text{diag}(\mathbf{D},\dots,\mathbf{D}), \\ \mathbf{b} \in \mathbb{R}^{n_k N^E_{\mathcal{K}}} &: \quad \mathbf{b} = [\mathbf{V}(:,1),\dots,\mathbf{V}(:,N^E_{\mathcal{K}})], \\ \boldsymbol{\omega} \in \mathbb{R}^{N^E_{\text{dof}}N^E_{\mathcal{K}}} &: \quad \boldsymbol{\omega} = [\mathbf{W}(:,1),\dots,\mathbf{W}(:,N^E_{\mathcal{K}})], \end{aligned}$$

$\lambda \in \mathbb{R}^{n_k N^E_{\mathcal{K}}}$ denotes the vector of Lagrangian multipliers associated with the constraint (23), $\mathbf{I} \in \mathbb{R}^{N^E_{\text{dof}}N^E_{\mathcal{K}}\times N^E_{\text{dof}}N^E_{\mathcal{K}}}$ is the identity matrix, $\mathbf{O} \in \mathbb{R}^{n_k N^E_{\mathcal{K}}\times n_k N^E_{\mathcal{K}}}$ is the zero matrix, and $\mathbf{0} \in \mathbb{R}^{N^E_{\text{dof}}N^E_{\mathcal{K}}}$ is the zero vector. The following result proves the nonsingularity of the linear system (24) under an appropriate choice of coarse nodes.

Proposition 1. *Given $N^E_{\text{dof}} \geq n_k$ and a choice of coarse nodes satisfying Theorem 1, problem (24) admits a unique solution and $\mathbb{P}_k(E) \subset \mathcal{V}_k(E)$.*

Proof. Observe that the optimization problem (24) is equivalent to

$$\begin{cases} 2\boldsymbol{\omega} + \mathbf{A}^T\lambda = \mathbf{0}, \\ \mathbf{A}\boldsymbol{\omega} = \boldsymbol{b}, \end{cases} \Leftrightarrow \begin{cases} \boldsymbol{\omega} = -\frac{1}{2}\mathbf{A}^T\lambda, \\ \mathbf{A}\boldsymbol{\omega} = \boldsymbol{b}, \end{cases} \Leftrightarrow \begin{cases} \boldsymbol{\omega} = -\frac{1}{2}\mathbf{A}^T\lambda, \\ \mathbf{A}\mathbf{A}^T\lambda = -2\boldsymbol{b}. \end{cases}$$

The matrix $\mathbf{A}\mathbf{A}^T$ is a non-singular block diagonal matrix, since its diagonal blocks are given by the squared non-singular matrix $\mathbf{D}\mathbf{D}^T$. Indeed, thanks to Theorem 1, matrix $\mathbf{D}$ is a full-rank matrix by rows, and, as a consequence, $\mathbf{D}\mathbf{D}^T$ is non-singular. Thus, the solution of problem (24) exists and is unique. □

By computing the Cholesky factorization [57] of the small matrix $\mathbf{D}\mathbf{D}^T$, it is possible to efficiently solve system (24), as detailed in Algorithm 1.

Algorithm 1: An algorithm to efficiently solve system (24).

Data: The matrices $\mathbf{D}$ and $\mathbf{V}$.
Result: The shape function weights $\mathbf{W}$.

```
L ← chol(DD^T) ;                    /* Compute Cholesky factorization of DD^T = LL^T once. */
for j = 1, ..., N^E_K do
    Ly = V(:, j) → y;
    L^T x = y → x;                  /* Solve two triangular systems of dimension n_k at each iteration. */
    W(:, j) ← D^T x;
end
```

Remark 2. In Algorithm 1, a rank-revealing factorization of $\mathbf{D}\mathbf{D}^T$ could be employed instead of the Cholesky factorization. This would enable an inline local test to verify that the chosen internal coarse nodes allow to reproduce polynomials.

Remark 3. For $k = 2$, we recall that a similar approach was already proposed in [50] to construct second-order shape functions. In that work, an optimization problem with the same cost functional but different constraints was solved to determine the shape function weights. Specifically, for $k = 2$, [50] considers the following minimization problem:

$$\min_{\mathbf{W}\in\mathbb{R}^{N^E_{\text{dof}}\times N^E_{\mathcal{K}}}} \sum_{i\in\mathcal{C}^E}\sum_{j\in\mathcal{K}^E} (\omega^E_{ij})^2 \tag{25}$$

$$\text{such that} \quad \sum_{i\in\mathcal{C}^E} \omega^E_{ij} = 1 \quad \forall j \in \mathcal{K}^E, \tag{26}$$

$$\boldsymbol{p}_j^E = \sum_{i \in C^E} \omega_{ij}^E \boldsymbol{x}_i^E \quad \forall j \in \mathcal{K}^E. \tag{27}$$

These constraints ensure that only the space of linear polynomials is contained in the final approximation space. For this reason, this construction is not sufficient to reproduce the desired convergence rate of $\mathbb{P}_2$-elements [50], since it only yields a linear convergence rate.

To overcome this limitation, [50] proposed replacing the cost functional (25) with the following variational energy functional:

$$\sum_{i \in C^E} \left[\sum_{e \in \mathcal{E}_{h,E,\mathcal{K}}} \int_e \|\nabla^+ \varphi_i^E - \nabla^- \varphi_i^E\|_2^2 + \epsilon \int_E \|\nabla \varphi_i^E\|_2^2 \right], \tag{28}$$

where $\mathcal{E}_{h,E,\mathcal{K}}$ denotes the set of virtual edges related to the element E, and the operators ∇_σ^+ and ∇_σ^+ correspond to the gradient with respect to the triangle on the right (+) and on the left (−) of the edge, respectively. The first term of the cost function (28) penalizes flux jumps, whereas the second one acts as a regularization term, which is needed since the flux matrix may be singular for non-simplicial cells.

By adopting this formulation, [50] achieved the expected convergence rate for $k = 2$. It is worth noting that the weights obtained through (28) generally produce smoother shape functions than ours, typically leading to slightly smaller error constants. However, extending problem (28) to higher polynomial orders is nontrivial, as it would require penalizing higher-order derivative jumps and properly balancing them within a single cost functional. Moreover, such an extension entails significantly higher computational cost.

5. The zipped discrete problem

In the following, we add a superscript E every time we want to highlight the dependency on the element E, whereas the same symbol without the superscript refers to its global counterpart. Moreover, we will use the same symbol C to denote a positive constant that does not depend on the mesh size h, with different meanings in different contexts.

Given the shape functions described in the previous section, we are now able to properly describe the final local zipped finite element space introduced in Eq. (6) as

$$\mathcal{V}_k(E) := \{v \in C^0(\overline{E}) \cap H^1(E) : (i)\ v \in \mathbb{P}_k(T) \quad \forall T \in \mathcal{T}_E, \tag{29}$$

$$(ii)\ v(\boldsymbol{p}_j^E) = \sum_{i \in C^E} \omega_{ij}^E \operatorname{dof}_i^E(v) \quad \forall j \in \mathcal{K}^E\}, \tag{30}$$

where the triangulation $\mathcal{T}_E$ is defined as in (9). We remark that $\mathbb{P}_k(E) \subset \mathcal{V}_k(E)$ due to Property 1.

On $\mathcal{V}_k(E)$, we choose the following set of degrees of freedom:

- **D.1** the values at the vertices of E;
- **D.2** if $k \geq 2$, the values in $k-1$ evenly spaced points internal of the edges of $e \in \mathcal{E}_{h,E}$;
- **D.3** if $k \geq 3$, the values in a set of internal nodes that allows to satisfy Theorem 1,

whose nodal coordinates correspond to the local coarse nodes $\{\boldsymbol{x}_i^E\}_{i \in C^E}$, as stated in (15).

Proposition 2. *The degrees of freedom* **D.1–D.3** *are unisolvent for* $\mathcal{V}_k(E)$.

Proof. We observe that the number of degrees of freedom is equal to the dimension of the space. To prove the unisolvence, we have to show that

$$\operatorname{dof}_i^E(v) = 0 \quad \forall i \in C^E \quad \Rightarrow \quad v = 0 \quad \forall v \in \mathcal{V}_k(E).$$

Thus, from the DOFs definition of Eq. (15), let us consider a generic function $v \in \mathcal{V}_k(E)$ such that

$$v(\boldsymbol{\xi}_i^E) = 0 \quad \forall i \in C^E. \tag{31}$$

Moreover, from Eqs. (30) and (31), it holds

$$v(\boldsymbol{\xi}_i^E) = 0 \quad \forall i \in \mathcal{K}^E. \tag{32}$$

Defined $\mathbb{V}(E; \mathcal{T}_E)$ as in (12), we observe that the evaluations of a function $v \in \mathcal{V}_k(E) \subset \mathbb{V}(E; \mathcal{T}_E)$ at the fine nodes, i.e. $v(\boldsymbol{\xi}_i^E)$, $\forall i \in \mathcal{F}^E$ constitute a set of unisolvent degrees of freedom for the space $\mathbb{V}(E; \mathcal{T}_E)$. Since $\mathcal{F}^E = C^E \cup \mathcal{K}^E$, Eqs. (31) and (32) imply $v = 0$. □

Proposition 3. *The Z-FEM functions defined in* (16) *satisfy the Kronecker-Delta Property* **P.2**.

Proof. We have to prove that $\operatorname{dof}_i^E(\varphi_j^E) = \delta_{ij}$ for all $i, j = 1, \dots, N_{\text{dof}}^E$. Thus, for all local DOFs, we have

$$\begin{aligned} \operatorname{dof}_i^E(\varphi_j^E) &= \varphi_j^E(\boldsymbol{x}_i^E) \\ &= \Psi_j^{\mathcal{T}_E}(\boldsymbol{x}_i^E) + \sum_{\ell \in \mathcal{K}^E} \omega_{j\ell}^E \Psi_\ell^{\mathcal{T}_E}(\boldsymbol{x}_i^E) \end{aligned}$$

$$= \delta_{ij} + \sum_{\ell=N^E_{\mathrm{dof}}+1}^{N^E_{\Psi,k}} \omega^E_{j\ell}\delta_{i\ell} = \delta_{ij} \qquad \forall i,j = 1,\dots,N^E_{\mathrm{dof}},$$

due to the Kronecker-Delta property of finite element basis functions with respect to the set of fine nodes. □

As done elementwise, we can define the global sets of coarse, virtual, and fine nodes as $\mathcal{C} = \bigcup_{E\in\Omega_h} \mathcal{C}^E$, $\mathcal{K} = \bigcup_{E\in\Omega_h} \mathcal{K}^E$, and $\mathcal{F} = \bigcup_{E\in\Omega_h} \mathcal{F}^E$, respectively. The fine nodes, in particular, represent the nodal coordinates for the finite element basis functions $\{\Psi_i\}_{i=1}^{N^{\Psi,\Omega}}$ that span the finite element space related to a triangulation of the entire domain Ω given by the union of local sub-triangulations $\{\mathcal{T}_E\}_{E\in\Omega_h}$. We observe that the global set of coarse nodes identifies the global Z-FEM degrees of freedom for the Z-FEM space (5). Specifically, for each $v \in \mathcal{V}_{h,k}$, we consider the following global DOFs:

- the values of v at the internal vertices of Ω_h,
- if $k \geq 2$, the values of v at $k-1$ equispaced points defined along each internal edge of Ω_h,
- if $k \geq 3$, the values at the set of internal nodes that allow to satisfy Theorem 1 in each element $E \in \Omega_h$.

Proposition 4. *The global Z-FEM basis functions $\{\varphi_i\}_{i=1}^{N_{\mathrm{dof}}}$ related to the global DOFs satisfy Property P.3, i.e. they are continuous all across the PDE domain $\overline{\Omega}$.*

Proof. We observe that Property **P.3** is satisfied by construction and by the continuity of the finite element basis functions associated with the fine nodes. In particular, all finite element basis functions associated with virtual nodes vanish on the boundaries ∂E for all E. Consequently, $\varphi_{i|\partial E} = \Psi_{i|\partial E}$ for all the coarse node $i = 1,\dots,N_{\mathrm{dof}}$. □

Remark 4. We observe that the shape functions $\{\varphi_i\}_{i=1}^{N^E_{\mathrm{dof}}}$ satisfy Properties **P.2** and **P.3** independently of the choice of the weights and internal coarse nodes.

Moreover, the Z-FEM shape functions satisfy the partition-of-unity property in addition to Properties **P.1**, **P.2**, and **P.3**.

Proposition 5. *The Z-FEM basis functions satisfy the partition-of-unity property, i.e.*

$$\sum_{i=1}^{N_{\mathrm{dof}}} \varphi_i(\boldsymbol{x}) = 1 \quad \forall \boldsymbol{x} \in \Omega. \tag{33}$$

Proof. Let us first consider a point $\boldsymbol{x}$ lying in the interior of an element $E \in \Omega_h$. The only Z-FEM basis functions with support on E are those associated with the elemental degrees of freedom $\{\mathrm{dof}_i^E : i = 1,\dots,N^E_{\mathrm{dof}}\}$. The first constraint of the optimization problem (25), which defines the shape-function weights, is equivalent to

$$\begin{aligned} 1 = m_1(\boldsymbol{p}_n^E) &= \sum_{i=1}^{N^E_{\mathrm{dof}}} \mathrm{dof}_i^E(1)\varphi_i^E(\boldsymbol{p}_n^E) \\ &= \sum_{i=1}^{N^E_{\mathrm{dof}}} \left[\Psi_i^{\mathcal{T}_E}(\boldsymbol{p}_n^E) + \sum_{j\in\mathcal{K}^E} \omega_{ij}^E \Psi_j^{\mathcal{T}_E}(\boldsymbol{p}_n^E) \right] = \sum_{i=1}^{N^E_{\mathrm{dof}}} \omega_{in}^E, \quad \forall n \in \mathcal{K}^E. \end{aligned}$$

Therefore, for a generic point $\boldsymbol{x} \in E$, we obtain

$$\begin{aligned} \sum_{m=1}^{N_{\mathrm{dof}}} \varphi_m(\boldsymbol{x}) = \sum_{i=1}^{N^E_{\mathrm{dof}}} \varphi_i^E(\boldsymbol{x}) &= \sum_{i=1}^{N^E_{\mathrm{dof}}} \left[\Psi_i^{\mathcal{T}_E}(\boldsymbol{x}) + \sum_{j\in\mathcal{K}^E} \omega_{ij}^E \Psi_j^{\mathcal{T}_E}(\boldsymbol{x}) \right] \\ &= \sum_{i\in\mathcal{C}^E} \Psi_i^{\mathcal{T}_E}(\boldsymbol{x}) + \sum_{j\in\mathcal{K}^E} \left(\sum_{i\in\mathcal{C}^E} \omega_{ij}^E \right) \Psi_j^{\mathcal{T}_E}(\boldsymbol{x}) \\ &= \sum_{i\in\mathcal{C}^E} \Psi_i^{\mathcal{T}_E}(\boldsymbol{x}) + \sum_{j\in\mathcal{K}^E} \Psi_j^{\mathcal{T}_E}(\boldsymbol{x}) = \sum_{k\in\mathcal{F}^E} \Psi_k^{\mathcal{T}_E}(\boldsymbol{x}) = 1, \end{aligned}$$

where the last equality follows from the fact that the standard FEM basis functions $\{\Psi_k^{\mathcal{T}_E}\}_{k\in\mathcal{F}^E}$ associated with the fine nodes satisfy the partition-of-unity property.

We now consider a point $\boldsymbol{x} \in e$, where e denotes an edge of the tessellation Ω_h. The only basis functions with support on e are those associated with the $k+1$ boundary degrees of freedom. Z-FEM basis functions are continuous across tessellation edges and, in particular, for each edge degree of freedom i, it holds

$$\varphi_{i|e} = \Psi_{i|e}, \tag{34}$$

where $\Psi_{i|e}$ denotes the corresponding FEM basis function defined on the sub-triangulation of Ω_h. Hence, for points $\boldsymbol{x}$ lying on edges of the tessellation, the partition-of-unity property of Z-FEM is directly inherited from the corresponding FEM property. The same argument applies to points $\boldsymbol{x}$ corresponding to the vertices of the tessellation. □

Given the global Z-FEM space defined in (5), the zipped discretization of problem (3) reads as: *Find* $u_h \in \mathcal{V}_{h,k}$ *such that*

$$\mathcal{B}(u_h, v_h) = \left(f, v_h\right)_\Omega \quad \forall v_h \in \mathcal{V}_{h,k}, \tag{35}$$

where u_h can be represented as $u_h = \sum_{i=1}^{N_{\text{dof}}} \text{dof}_i(u)\varphi_i$. Thus, problem (35) is equivalent to solving the following symmetric linear system

$$\boldsymbol{A}\boldsymbol{u} = \boldsymbol{f}, \tag{36}$$

where $\boldsymbol{u} \in \mathbb{R}^{N_{\text{dof}}}$ collects the DOFs $\{\text{dof}_i(u)\}_{i=1}^{N_{\text{dof}}}$, while the entries of the symmetric matrix $\boldsymbol{A} \in \mathbb{R}^{N_{\text{dof}} \times N_{\text{dof}}}$ and the right hand side $\boldsymbol{f} \in \mathbb{R}^{N_{\text{dof}}}$, for all $i, j = 1, \dots, N_{\text{dof}}$, are defined as

$$\boldsymbol{A}_{ij} = \mathcal{B}(\varphi_j, \varphi_i) = \int_\Omega \boldsymbol{\kappa} \nabla\varphi_i \cdot \nabla\varphi_j + \int_\Omega \gamma \varphi_i \ \varphi_j, \qquad \boldsymbol{f}_i = \int_\Omega f \varphi_i. \tag{37}$$

As in the standard FEM formulation, the existence and uniqueness of the solution of problem (35) are inherited by the continuous framework. Moreover, the continuity and the coercivity of the bilinear form $\mathcal{B}$ on $\mathcal{V}_{h,k} \subset \mathcal{V}$ are the key ingredients for Céa's Lemma [2]:

$$\|u - u_h\|_{H^1(\Omega)} \leq C \min_{v_h \in \mathcal{V}_{h,k}} \|u - v_h\|_{H^1(\Omega)}, \tag{38}$$

where C is a constant related to continuity and coercivity constants of $\mathcal{B}$ on $\mathcal{V}$.

Proposition 6. *Under mesh Assumption 1, let* $u \in H^{k+1}(\Omega)$, $k \geq 1$, *be the solution of (3), and let* $u_h \in \mathcal{V}_{h,k}$ *be the solution of the discrete problem (35). It holds:*

$$\|u - u_h\|_{H^1(\Omega)} \leq C h^k |u|_{H^{k+1}(\Omega)}, \tag{39}$$

and

$$\|u - u_h\|_{L^2(\Omega)} \leq C h^{k+1} |u|_{H^{k+1}(\Omega)}. \tag{40}$$

Proof. Let us consider an element $E \in \Omega_h$. Let us define the interpolation operator $\mathcal{I}_k^E : C^0(\overline{E}) \to \mathcal{V}_k(E)$ for all $E \in \Omega_h$:

$$\mathcal{I}_k^E v := \sum_{i \in \mathcal{C}^E} \text{dof}_i(v)\varphi_i. \tag{41}$$

We define the set of coarse nodes that belong to triangle $T \in \mathcal{T}_E$ as $\mathcal{C}_T^E \subset \mathcal{C}^E$ and the virtual nodes that belong to triangle $T \in \mathcal{T}_E$ as $\mathcal{K}_T^E \subset \mathcal{K}^E$. The interpolation operator $\mathcal{I}_k^T : C^0(\overline{T}) \to \mathbb{P}_k(T)$ on $T \in \mathcal{T}_E$ is defined as the restriction of (41) on T:

$$\begin{aligned}
\mathcal{I}_k^T v &:= \sum_{i \in \mathcal{C}_T^E} \text{dof}_i(v)\varphi_i|_T \\
&= \sum_{i \in \mathcal{C}_T^E} \text{dof}_i(v)[\Psi_i|_T + \sum_{j \in \mathcal{K}_T^E} \omega_{ij}\Psi_j|_T] \\
&= \sum_{j \in \mathcal{C}_T^E \cup \mathcal{K}_T^E} \overline{\text{dof}}_j(v)\Psi_j|_T \qquad \forall v \in H^1(T),
\end{aligned}$$

where $\{\overline{\text{dof}}_j(v)\}_{j \in \mathcal{C}_T^E \cup \mathcal{K}_T^E}$ are defined as: $\forall v \in C^0(\overline{T})$

$$\overline{\text{dof}}_i(v) := \begin{cases} \text{dof}_i(v), & i \in \mathcal{C}_T^E, \\ \displaystyle\sum_{\ell \in \mathcal{C}_T^E} \omega_{\ell i} \, \text{dof}_\ell(v), & i \in \mathcal{K}_T^E. \end{cases}$$

Note that if $v \in H^{k+1}(T)$, then $\mathcal{I}_k^T v \in H^{k+1}(T)$. Moreover, since $\mathbb{P}_k(E) \subseteq \mathcal{V}_k(E)$, then $p = \mathcal{I}_k^E p$ and $p_{|T} = \left(\mathcal{I}_k^E p\right)_{|T} = \mathcal{I}_k^T p$ for all $p \in \mathbb{P}_k(E)$. Thus, from Theorem 4.4.4 in [2], it follows that:

$$|u - \mathcal{I}_k^T u|_{H^1(T)} \leq C h_T^k |u|_{H^{k+1}(T)}.$$

The mesh Assumption 1 imply that the triangles belonging to $\mathcal{T}_E$ of an element $E \in \Omega_h$ are regular (see Remark 1).
Now, by Theorem 4.4.20 in [2], we derive the following estimate on $E \in \Omega_h$, since $(u - \mathcal{I}_k^E u) \in H^1(E)$,

$$\begin{aligned}
\|u - \mathcal{I}_k^E u\|_{H^1(E)}^2 &= \sum_{T \in \mathcal{T}_E} \|u - \mathcal{I}_k^T u\|_{H^1(T)}^2 \\
&\leq C \left(\max_{T \in \mathcal{T}_E} h_T\right)^{2k} \sum_{T \in \mathcal{T}_E} |u|_{H^{k+1}(T)}^2 \\
&\leq C h_E^{2k} |u|_{H^{k+1}(E)}^2.
\end{aligned}$$

Thus,

$$\|u - \mathcal{I}_k u\|_{H^1(\Omega)} \leq C h^k |u|_{H^{k+1}(\Omega)}, \tag{42}$$

where $(\mathcal{I}_k)_{|E} = \mathcal{I}_k^E$ for all $E \in \Omega_h$.

From Céa's Eq. (38), we have

$$\|u - u_h\|_{H^1(\Omega)} \leq C \min_{v_h \in \mathcal{V}_{h,k}} \|u - v_h\|_{H^1(\Omega)} \leq C \|u - \mathcal{I}_k u\|_{H^1(\Omega)} \leq C h^k |u|_{H^{k+1}(E)}. \tag{43}$$

Eq. (39) follows.

The L^2-norm estimate follows from a duality argument. Let Ω be a convex domain and let us define the adjoint operator related to the problem (1) as $\mathcal{L}^* w := -\nabla \cdot (\boldsymbol{\kappa} \nabla w) + \gamma w$. For every $g \in L^2(\Omega)$, there exists a unique $w \in H^2(\Omega) \cap \mathcal{V}$ such that

$$\mathcal{L}^* w = g, \tag{44}$$

and

$$\|w\|_{H^2(\Omega)} \leq C \|g\|_{L^2(\Omega)}, \tag{45}$$

with a constant C independent of g and h [58]. Let ϕ be the solution of the adjoint problem (44) associated with the right-hand side $g = u - u_h$. Using Galerkin Orthogonality, continuity of $\mathcal{B}$, and the results (42) and (45), it holds,

$$\begin{aligned}
\|u - u_h\|^2_{L^2(\Omega)} &= \left(u - u_h, g\right)_\Omega = \mathcal{B}(u - u_h, \phi) \\
&= \mathcal{B}(u - u_h, \phi - \mathcal{I}_k \phi) \\
&\leq C \|u - u_h\|_{H^1(\Omega)} \|\phi - \mathcal{I}_k \phi\|_{H^1(\Omega)} \\
&\leq C h \|u - u_h\|_{H^1(\Omega)} \|\phi\|_{H^2(\Omega)} \\
&\leq C h \|u - u_h\|_{H^1(\Omega)} \|u - u_h\|_{L^2(\Omega)}.
\end{aligned}$$

By simplifying the previous equation and using (43), the thesis follows. □

6. Numerical experiments

In this section, we show various numerical experiments to assess the performance of the zipped finite element method. In Section 6.1 we prove that the polynomials can be effectively represented as linear combinations of the Z-FEM basis functions, whereas in Section 6.2 we solve problem (1) and compare the method with FEM and VEM on general polygonal meshes. Finally, Section 6.3 provides a numerical experiment over Discrete Fracture Networks, showcasing the capability of Z-FEM of handling more complex geometries.

6.1. Test 1: Polynomials approximation

The first test we propose aims to show how accurately the local basis functions are able to reproduce polynomials. For this purpose, we consider a set of different polygons and, on each polygon, we compute the following polynomial approximation errors

$$\mathrm{err}_{I,0} = \max_{\alpha=1,\dots,n_k} \|m_\alpha - \mathcal{I}_k^E m_\alpha\|_{L^2(E)}, \quad \mathrm{err}_{I,\nabla} = \max_{\alpha=1,\dots,n_k} \|\nabla m_\alpha - \nabla \mathcal{I}_k^E m_\alpha\|_{L^2(E)}, \tag{46}$$

where the interpolator $\mathcal{I}_k^E$ is defined in (41).

Examples from the tested cases are shown in Table 2. These tested cases include polygons sampled from diverse classes: the reference triangle, a regular nonagon, an irregular quadrilateral, an irregular concave polygon, a star, and, finally, a general polygon with hanging nodes. For each one, we draw in the top part of Table 2 the considered polygon and its sub-triangulation, represented by assigning a different color to each sub-triangle. Moreover, for each order $k = 1, \dots, 6$, we report in such a table the errors $\mathrm{err}_{I,0}$ and $\mathrm{err}_{I,\nabla}$, computed as defined in (46). In all tested cases, both errors are found to be very small, mostly between 10^{-10} and 10^{-16}, with a single exception around 10^{-8} given by the distorted concave octagon for the highest order $k = 6$. This demonstrates that the proposed shape functions can approximate polynomials with very high accuracy, despite the use of the heuristic choice for the internal degrees of freedom described in Section 4. Moreover, we emphasize that the matrices $\mathbf{D}$ related to these experiments have always full rank, thereby confirming that the assumptions of Property 1 are satisfied also in the case of the proposed heuristic selection of internal coarse nodes for all the tested cases.

We remark that the choice of the internal coarse nodes has a crucial impact on the performance of the proposed element. We recall that the heuristic algorithm introduced in Section 4.2 selects the internal coarse nodes with the dual objective of avoiding node alignment and promoting a homogeneous spatial distribution. To highlight this aspect, Table 3 presents four different selections of internal coarse nodes for a triangle with three hanging nodes and polynomial degree $k = 6$, together with the corresponding polynomial approximation errors (46). In this configuration, the matrix $\mathbf{D}$ in Algorithm 1 has size $n_k \times N_{\mathrm{dof}}^E = 28 \times 46$. Therefore, we need 28 singular values of $\mathbf{D}$ to be strictly positive to guarantee the solvability of Algorithm 1. For each configuration, we report in the table the value $\sigma_r(\mathbf{D})$ of the 28-th smallest singular value of $\mathbf{D}$. In the first case (top-left), the $n_{k-3} = 10$ internal coarse

Table 2
Test 1: Polynomial approximation errors (46) over different polygons for different orders.

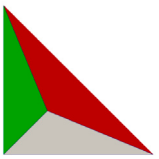

Triangle
$N_v^E = 3$

k	$\mathrm{err}_{I,0}$	$\mathrm{err}_{I,\nabla}$
1	1.8326e-17	5.7941e-16
2	2.8347e-16	2.9336e-15
3	1.2973e-15	1.8339e-14
4	5.8797e-14	7.3820e-13
5	9.1859e-14	3.3798e-12
6	5.6793e-13	1.4408e-11

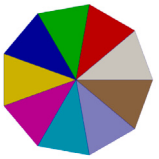

Regular
$N_v^E = 9$

k	$\mathrm{err}_{I,0}$	$\mathrm{err}_{I,\nabla}$
1	2.6949e-16	2.8693e-16
2	1.3028e-14	8.5565e-14
3	1.1445e-14	8.9299e-14
4	1.8168e-14	2.6553e-13
5	4.7007e-14	5.7959e-13
6	1.5337e-13	2.1020e-12

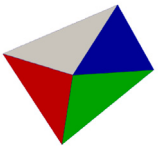

Irregular
$N_v^E = 4$

k	$\mathrm{err}_{I,0}$	$\mathrm{err}_{I,\nabla}$
1	6.3167e-17	2.3435e-16
2	8.2278e-16	4.2732e-15
3	8.9258e-16	6.2626e-15
4	9.6685e-15	9.3015e-14
5	3.0512e-14	4.0792e-13
6	1.9029e-13	4.1390e-12

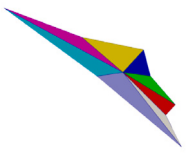

Concave
$N_v^E = 8$

k	$\mathrm{err}_{I,0}$	$\mathrm{err}_{I,\nabla}$
1	1.8493e-17	3.0149e-16
2	2.1022e-16	1.2040e-14
3	3.6450e-15	2.0565e-13
4	1.6660e-13	1.9650e-11
5	1.3747e-12	1.2459e-10
6	3.9631e-11	1.0054e-08

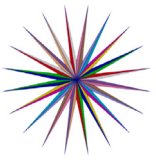

Star
$N_v^E = 40$

k	$\mathrm{err}_{I,0}$	$\mathrm{err}_{I,\nabla}$
1	2.8739e-16	6.1237e-15
2	2.3066e-16	1.9867e-14
3	2.1459e-16	3.6148e-14
4	5.6569e-16	1.5407e-13
5	3.4445e-15	5.2178e-13
6	7.2247e-15	2.1387e-12

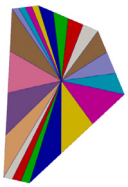

Hexagon
with hanging nodes
$N_v^E = 21$

k	$\mathrm{err}_{I,0}$	$\mathrm{err}_{I,\nabla}$
1	7.1691e-17	7.1416e-16
2	1.6957e-15	1.8354e-14
3	2.6098e-15	1.4942e-13
4	3.2337e-14	8.2584e-13
5	3.3556e-14	4.4693e-12
6	6.3862e-13	4.8157e-11

nodes satisfy the assumptions of Theorem 1. As expected, $\sigma_r(\mathbf{D})$ is strictly positive, ensuring solvability of Algorithm 1 and high accuracy in polynomial reproducibility. The second configuration (top-right), obtained through the proposed heuristic procedure, yields results that are fully comparable with those achieved under the theoretical assumptions of Theorem 1, both in terms of polynomial consistency errors and conditioning of $\mathbf{D}$. In the third case (bottom-left), the internal coarse nodes are aligned along a straight line. This geometric degeneracy leads to $\sigma_r(\mathbf{D})$ being nearly zero. As a consequence, the Algorithm 1 cannot be applied because $\mathbf{D}$ is rank-deficient. Finally, in the fourth case (bottom-right), the nodes do not follow a homogeneous spatial distribution. Although the matrix $\mathbf{D}$ has maximum rank, the conditioning deteriorates and the polynomial approximation errors increase, resulting in suboptimal performance. In conclusion, these experiments clearly highlight the relevance of node placement and support the effectiveness of the proposed heuristic strategy.

6.2. Test 2: Convergence rates

Let us consider problem (1), where the diffusion and reaction coefficients are defined as

$$\boldsymbol{\kappa}(\boldsymbol{x}) = \begin{bmatrix} 1+x_2^2 & -x_1x_2 \\ -x_1x_2 & 1+x_1^2 \end{bmatrix}, \quad \gamma(\boldsymbol{x}) = x_1x_2.$$

We choose the forcing term and the Dirichlet boundary condition in accordance with the exact solution:

$$u(\boldsymbol{x}) = \sin(2\pi x_1)\sin(2\pi x_2).$$

Table 3
Test 1: Four different choices for internal coarse nodes in the case of a triangle with three hanging nodes for $k = 6$. The caption below each figure reports the polynomial approximation errors (46) and the smallest singular values of the matrix $\mathbf{D}$ defining the constraints of the optimization problem (22)–(23). Top-left: A configuration satisfying the assumptions of Theorem 1. Top-right: The configuration obtained using the proposed heuristic procedure. Bottom-left: Effect of node alignment. In this case, "–" indicates that Algorithm 1 cannot be applied because $\mathbf{D}$ is rank-deficient. Bottom-right: Effect of non-homogeneous spatial distribution of the coarse nodes.

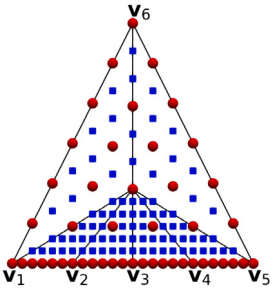

k	$\mathrm{err}_{I,0}$	$\mathrm{err}_{I,\nabla}$	$\sigma_r(\mathbf{D})$
6	1.2261e-13	3.6235e-12	4.5635e-05

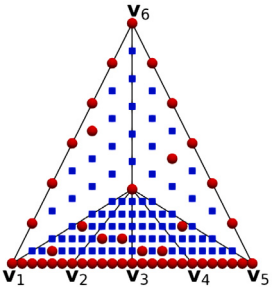

k	$\mathrm{err}_{I,0}$	$\mathrm{err}_{I,\nabla}$	$\sigma_r(\mathbf{D})$
6	1.3427e-11	6.3805e-10	5.7551e-06

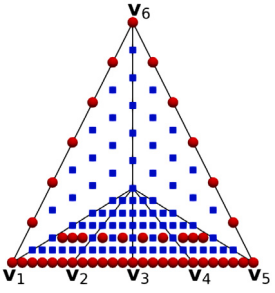

k	$\mathrm{err}_{I,0}$	$\mathrm{err}_{I,\nabla}$	$\sigma_r(\mathbf{D})$
6	–	–	7.2575e-19

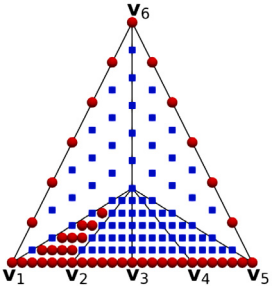

k	$\mathrm{err}_{I,0}$	$\mathrm{err}_{I,\nabla}$	$\sigma_r(\mathbf{D})$
6	1.7738e-07	3.6310e-06	5.0059e-08

In this test case, we assess the performance of the proposed method by solving this problem on different families of meshes. For each family of meshes, we compute the following standard errors:

$$\mathrm{err}_0 = \|u - u_h\|_{L^2(\Omega)}, \qquad \mathrm{err}_\nabla = \|\nabla u - \nabla u_h\|_{L^2(\Omega)}, \tag{47}$$

as the mesh size h decreases (thus, as $N_{\mathrm{dof}} = \dim \mathcal{V}_{h,k}$ increases) and for $k = 1, \dots, 5$.

Specifically, we consider the following four mesh families:

- A family of randomly distorted quadrilateral meshes, obtained by perturbing the vertices of standard Cartesian grids;
- A family of Voronoi meshes generated using [59,60];
- The "Structured Concave" family of meshes available in the PolyDiM repository [51];
- The "Delaunay" family of meshes generated using [59,61].

The finest mesh for each family is depicted in Fig. 4 (see Fig. 5).

The results show that the errors decrease with the expected convergence rates, in agreement with the theoretical estimates given in (39) and (40).

For comparison purposes, we also include the errors obtained by solving problem (1) using a well-established polytopal approach, namely the Virtual Element Method [58], built on the same polygonal meshes. Additionally, for the polygonal families of meshes, namely Random Distorted, Voronoi, and Structured Concave, we report the results obtained with a standard Finite Element Method applied to the mesh generated by the union of zipped sub-triangulations. As highlighted by these results, the Z-FEM performance is comparable with that of standard VEM and FEM. Moreover, it is important to note that, with respect to VEM, the convergence curves indicate that Z-FEM achieves similar accuracy with slightly fewer degrees of freedom.

We observe that, on Delaunay meshes, Z-FEM and standard FEM differ in the choice of internal degrees of freedom for $k > 3$: Z-FEM selects them through the heuristic procedure described in Section 4.2, whereas FEM uses the standard algorithm shown in Fig. 2(b). Nonetheless, despite this difference, the performance of Z-FEM and FEM remains very similar.

We emphasize that the Z-FEM method has been deliberately designed to remain fully compatible with standard FEM technology. In particular, whenever a simplicial mesh is available, the use of a classical FEM discretization is naturally preferable. The Z-FEM formulation can instead be employed on the subset of non-simplicial elements, thereby providing a seamless strategy for the treatment of hybrid meshes composed of both triangular and general polygonal elements.

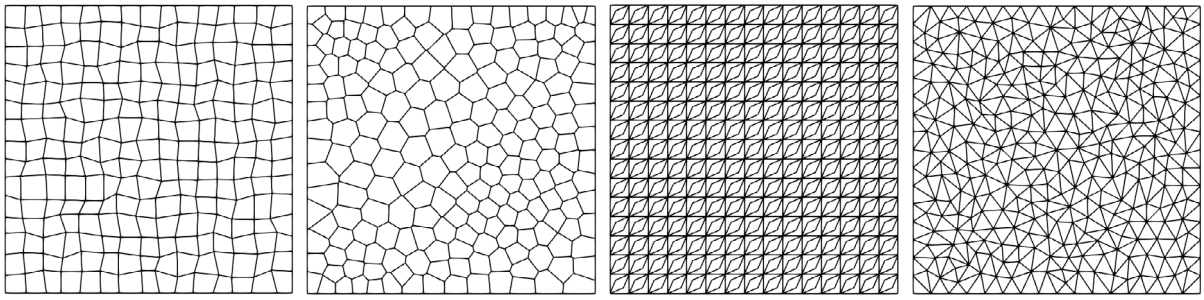

(a) Random Distorted. (b) Voronoi. (c) Structured Concave. (d) Delaunay.

Fig. 4. Test 2: Last refinement for each family of meshes employed.

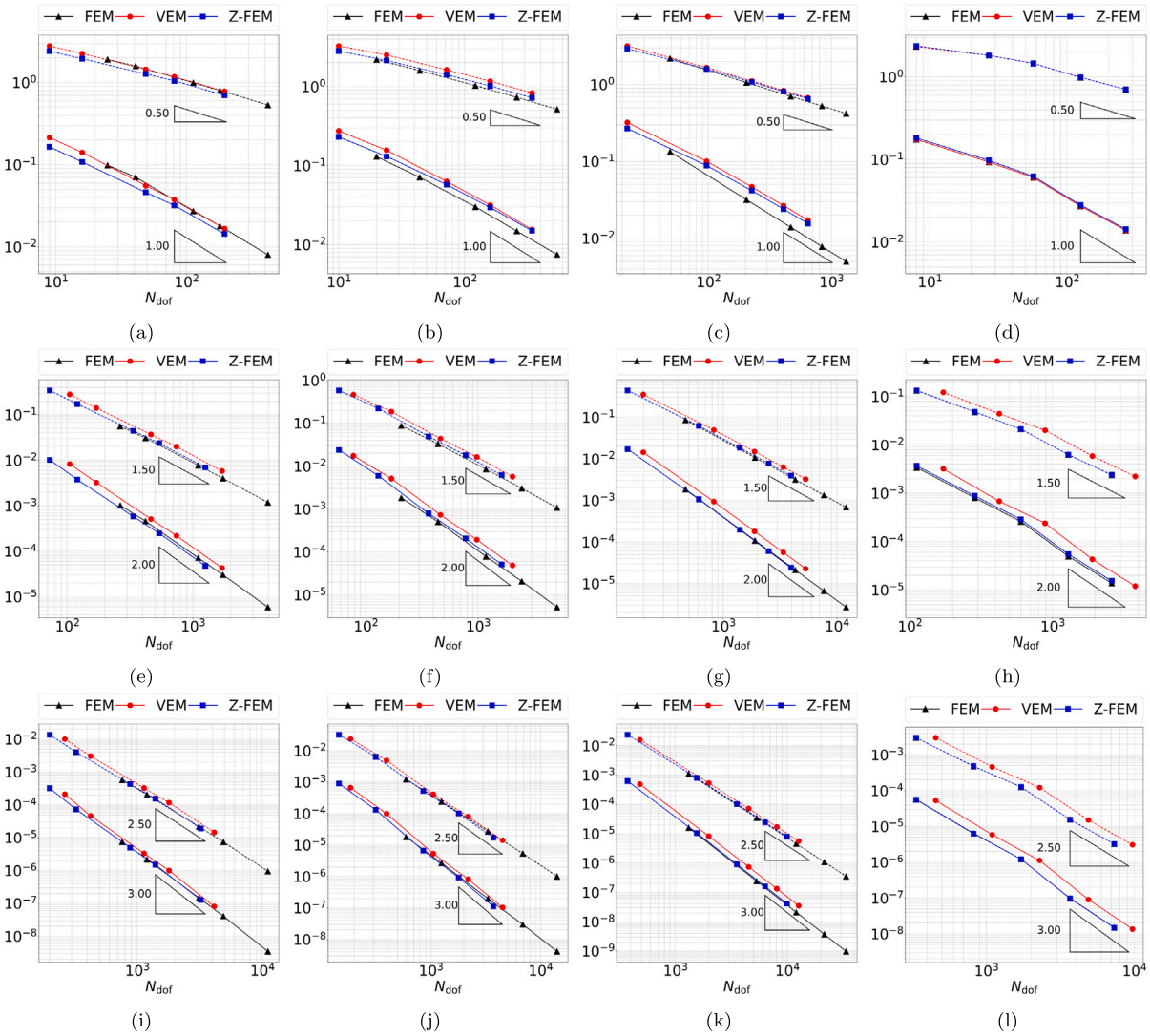

Fig. 5. Test 2: Behavior of errors (47) as N_{dof} increases. Each column corresponds to a different family of meshes. First column: Random Distorted. Second column: Voronoi. Third column: Structured Concave. Fourth column: Delaunay. Each row refers to a different value of $k = 1, 3, 5$. Solid lines: L^2-errors. Dashed lines: H^1-errors. For comparison purposes, FEM are built over the zipped sub-triangular meshes for the polygonal families of Random Distorted, Voronoi, and Structured Concave.

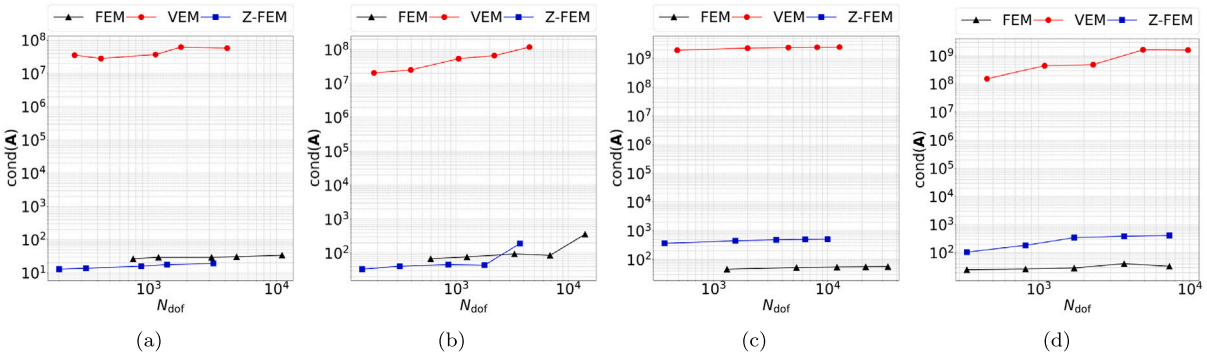

Fig. 6. Test 2: Behavior of the condition number of the global system matrix $\mathbf{A}$ as N_{dof} increases, for $k = 5$. Each column corresponds to a different family of meshes. First column: Random Distorted. Second column: Voronoi. Third column: Structured Concave. Fourth column: Delaunay. For comparison purposes, FEM are built over the zipped sub-triangular meshes for the polygonal families of Random Distorted, Voronoi, and Structured Concave.

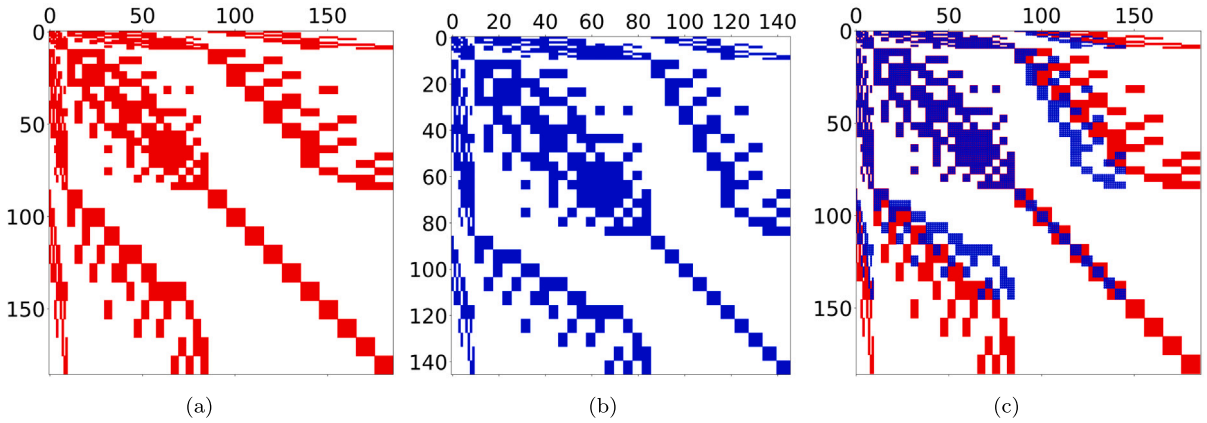

Fig. 7. Test 2: Sparsity pattern for the finest mesh of the Voronoi family for $k = 5$. Left: VEM. Center: Z-FEM. Right: Overlapped.

Concerning VEM, we recall that the standard enhanced VEM space [58] used here coincides with FEM for $k = 1$, but becomes larger for higher orders, requiring more degrees of freedom. It is also worth noting that, on triangles, FEM coincides with the Serendipity version of VEM [53] for every $k \geq 1$.

We observe that the proposed method achieves improved efficiency in terms of the number of degrees of freedom when compared with the standard VEM, while still retaining the capability to operate on general polygonal meshes. It is worth emphasizing, however, that the geometric assumptions underlying the present analysis are more restrictive. Indeed, the standard VEM framework is known to accommodate more general configurations, including elements that can be represented as the union of a finite number of star-shaped subdomains. In contrast, our theoretical framework is developed under the assumption that each mesh element is star-shaped, although it can be extended straightforwardly to elements that are a union of a finite number of star-shaped polygons. Moreover, the zipped formulation proposed here presents a structural simplification with respect to the classical VEM approach, as it does not require the introduction of problem-dependent stabilization terms or the construction of polynomial projection operators. These ingredients, which are central in standard VEM formulations, may introduce additional complexity when dealing with nonlinear problems or during post-processing phases.

In Fig. 6, we report the behavior of the condition number of the global discrete matrix $\mathbf{A}$ as N_{dof} increases for $k = 5$, for all the methods and families of meshes. We highlight that, as in standard FEM, the symmetry and overall structure of the zipped discrete system are inherited directly from the continuous problem. Moreover, the condition number of the Z-FEM is comparable with that of FEM in all the experiments we carried out. The sparsity pattern of the zipped global discrete matrix $\mathbf{A}$, instead, is dictated by the mesh connectivity and it is very similar to that of the Virtual Element Method, while having fewer internal DOFs, since both VEM and Z-FEM are C^0-conforming polygonal methods, as shown in Fig. 7.

6.3. Test 3: A benchmark problem on a discrete fracture network

To show the performance of the method in a more complex scenario, in this test we simulate the state of equilibrium of the hydraulic head u of a single–phase fluid flow inside a fractured medium. See e.g. [62] for more details. We consider the rock

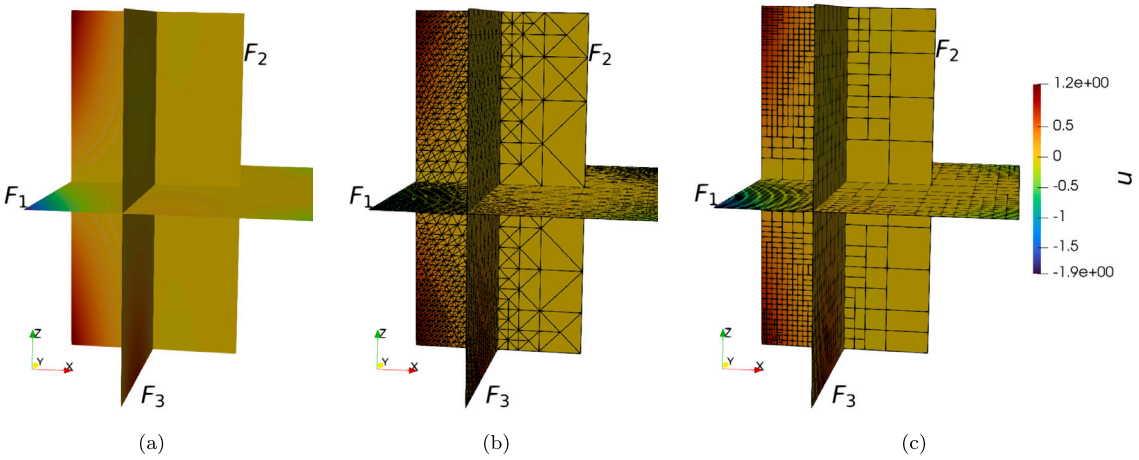

Fig. 8. Test 3: Domain description and mesh examples colored by the exact solution u. Left: DFN domain. Center: Third triangular refinement. Right: Third polygonal refinement.

surrounding the fractures as impervious and model the flow by Darcy's law. The medium is approximated by the Discrete Fracture Network (DFN) model. In this framework, the involved N^{Ω} fractures are assumed to have a negligible thickness with respect to the other dimensions, and are represented as planar polygons F_i, $i = 1, \dots, N^{\Omega}$, intersecting each other in a three-dimensional space. The domain Ω is the union of such fractures. Non-empty fracture intersections are denoted by $S_{ij} = F_i \cap F_j$. We set $S = \cup_{i,j} S_{ij}$.

Here, we consider the benchmark problem detailed in [62]. This benchmark consists of $N^{\Omega} = 3$ fractures as shown in Fig. 8(a). Despite being a simple network, it presents two geometrical features (a trace intersection and a trace tip) which make it worthwhile to analyze the behavior of the method at tackling them, while making us able to build an exact solution to evaluate the method performance. The computational domain $\Omega = F_1 \cup F_2 \cup F_3$ is defined by

$$
\begin{aligned}
F_1 &= \{(x_1, x_2, x_3) \in \mathbb{R}^3 : \ -1 \le x_1 \le \frac{1}{2}, \ -1 \le x_2 \le 1, \ x_3 = 0\},\\
F_2 &= \{(x_1, x_2, x_3) \in \mathbb{R}^3 : \ -1 \le x_1 \le 0, \ -1 \le x_3 \le 1, \ x_2 = 0\},\\
F_3 &= \{(x_1, x_2, x_3) \in \mathbb{R}^3 : \ -1 \le x_2 \le 1, \ -1 \le x_3 \le 1, \ x_1 = \frac{1}{2}\}.
\end{aligned}
$$

Let $\boldsymbol{n}^*_{i,ij}$ represent the outward unit normal at S_{ij} tangent to F_i for each side $\{+,-\}$ (left and right). For all $i, j = 1, \dots, N^{\Omega}$, the problem reads as [62]

$$
\begin{cases}
\nabla \cdot (-\nabla u_i) = f_i & \text{in } F_i \setminus S,\\
u_i = u_{D,i} & \text{on } \partial F_i,\\
u_{i|S^+_{ij}} = u_{i|S^-_{ij}} = u_{j|S^+_{ij}} = u_{j|S^-_{ij}} & \text{on } S_{ij},\\
\sum_{*\in\{+,-\}} (\nabla u_i \cdot \boldsymbol{n}^*_{i,ij})_{|S^*_{ij}} + (\nabla u_j \cdot \boldsymbol{n}^*_{j,ij})_{|S^*_{ij}} = 0 & \text{on } S_{ij},
\end{cases}
\tag{48}
$$

where the differential operator ∇ is defined on the tangent space F_i. The last two conditions in (48) represent continuity of the hydraulic head and mass conservation, respectively. This problem is characterized by a non-homogeneous Dirichlet boundary condition u_D on the whole boundary $\partial\Omega$ and a load term f_i on each fracture F_i, defined in accordance with the exact solution:

$$
\begin{aligned}
u_1(x_1, x_2, x_3) &= \frac{1}{10}\left(-x_1 - \frac{1}{2}\right)\left(8 x_1 x_2 \left(x_1^2 + x_2^2\right) \operatorname{arctan2}(x_2, x_1) + x_1^3\right) && \text{in } F_1,\\
u_2(x_1, x_2, x_3) &= \frac{1}{10}\left(-x_1 - \frac{1}{2}\right) x_1^3 - \frac{4}{5}\pi \left(-x_1 - \frac{1}{2}\right) x_1^3 |x_3| && \text{in } F_2,\\
u_3(x_1, x_2, x_3) &= (x_2 - 1) x_2 (x_2 + 1)(x_3 - 1) x_3 && \text{in } F_3,
\end{aligned}
$$

where $\operatorname{arctan2}(x_2, x_1)$ is the four-quadrant inverse tangent function with 2 arguments, that returns the appropriate quadrant of the computed angle x_2/x_1 [62].

When performing simulations on complex (or large) DFNs, the main problem to be addressed is the geometrical treatment of the domain, in particular when the global conformity of the mesh is required [63]. Different procedures can be applied to generate a family of polygonal meshes that are conforming at interfaces. A possible way consists in generating meshes independently for each fracture, regardless of the trace positions, and exploiting the capability of polygonal methods to handle aligned edges to recover the global conformity [63]. As an alternative, one may start from a minimal global mesh that is conforming at the interfaces, and then refine it while preserving the conformity [64]. Again, the ability to handle polygons with hanging nodes is beneficial to avoid over-propagating the refinement strategy to the neighbors of the marked cells. In this test, we adopt the triangular and polygonal

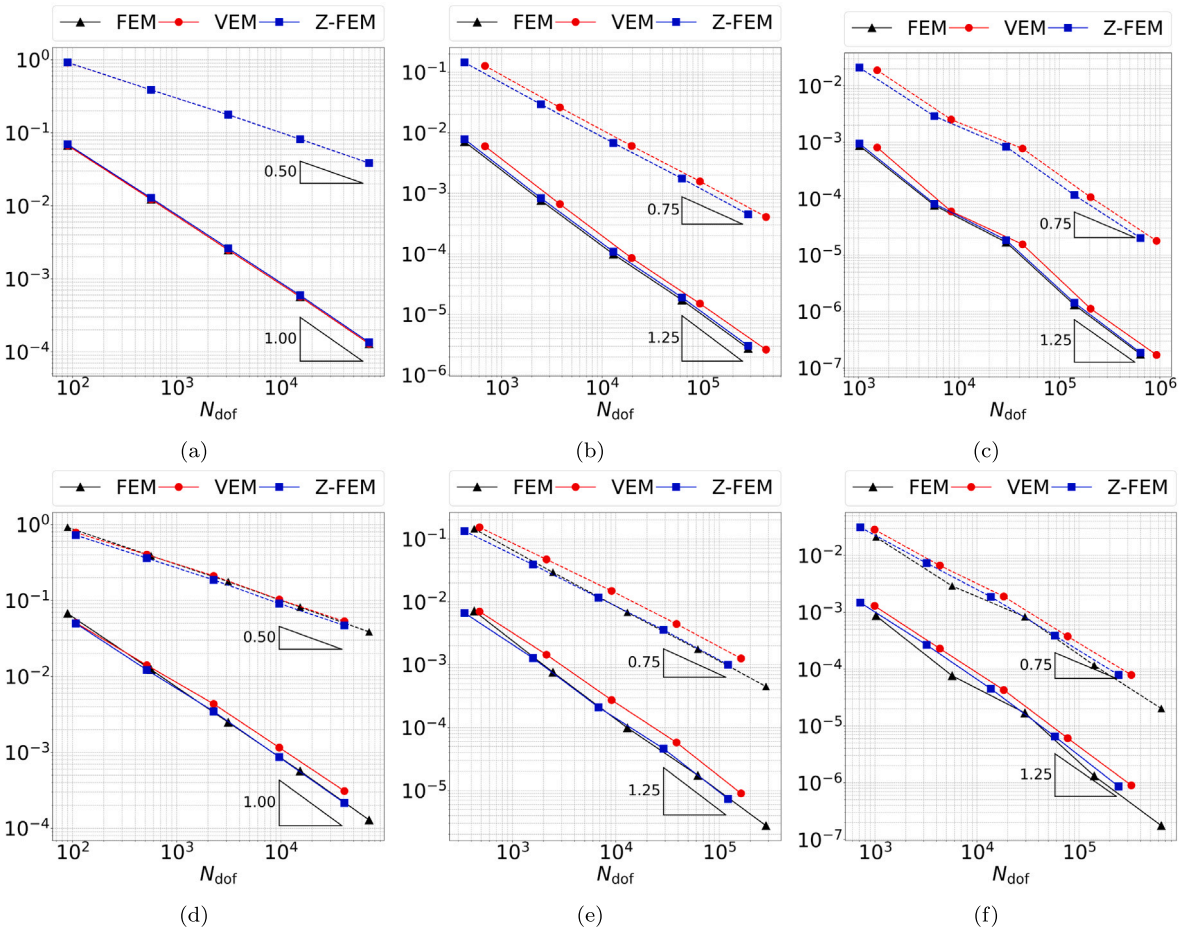

Fig. 9. Test 3: Behavior of errors (47) as N_{dof} increases. Each row corresponds to a different family of meshes. Top: conformed triangular. Bottom: conformed polygonal. Each column refers to a different value of $k = 1, 2, 3$. Solid lines: L^2-errors. Dashed lines: H^1-errors. For comparison purposes, in both rows, FEM are built over a family of triangular meshes with comparable mesh sizes h.

refinements generated for the same benchmark in [64], for $k = 1$, by using FEM and VEM a posteriori theory, respectively. We observe that the generation of a triangular mesh for this DFN is possible due to the simplicity of its geometry. For more realistic networks, the generation of good-quality triangular tessellation is usually unfeasible [64]. The families of employed meshes comprise 5 meshes each and are available in the paper GitHub repository. Figs. 8(b) and 8(c) show the third refinement for each family of meshes.

Denoting by $\widetilde{\Omega} := \Omega \setminus S$ the domain without the fracture intersections, the regularity of the solution is such that $u \in H^2(\widetilde{\Omega})$, but $u \notin H^3(\widetilde{\Omega})$ [62]. The regularity of the solution u limits the convergence rates for conforming methods like FEM, VEM, and Z-FEM. More precisely, based on the numerical results, the empirical orders of convergence for all the methods follow:

$$\text{err}_0 = O(N_{\text{dof}}^{-0.5\min\{2.5,k+1\}}), \quad \text{err}_\nabla = O(N_{\text{dof}}^{-0.5\min\{1.5,k\}}). \tag{49}$$

In Fig. 9, we report the behavior of errors (47) as N_{dof} increases. For comparison purposes, for the case of a polygonal family of meshes, we report the Z-FEM and VEM performance obtained on this mesh and the FEM behavior computed on the triangular meshes of comparable mesh sizes. As shown in this figure, even in the presence of a singular solution, the zipped method satisfies the theoretical properties inherited from the finite element method, and its performance is comparable to that of both FEM and VEM in terms of accuracy.

7. Conclusion

In this paper, we define a novel procedure to compute high-order shape functions over generic polygonal meshes, introducing a novel polygonal finite element method called Zipped Finite Element Method.

These shape functions are given by a linear combination of FEM basis functions, defined on a trivial sub-triangulation of each element of a generic polygonal mesh. We present a detailed analysis on the choice of the coefficients of such a combination. In

particular, these coefficients can be efficiently computed by solving a local optimization problem, whose solution can be cheaply obtained by solving a block-diagonal linear system with a single repeated factorizable block. We have demonstrated that, using a particular distribution of degrees of freedom, the solution of the optimization problem allows to retrieve all polynomials up to the specified order as a linear combination of the Z-FEM basis functions. We also highlight that, since the explicit form of the involved basis functions is available, this new formulation provides a way to obtain a finite element space that preserves all the theoretical properties of the FEM framework, but on more generic star-shaped polygons.

Numerical results confirm that our basis functions are able to reproduce polynomials and show optimal performance in terms of standard errors.

CRediT authorship contribution statement

Stefano Berrone: Writing – review & editing, Supervision, Resources, Project administration, Formal analysis. **Lorenzo Neva:** Writing – review & editing, Writing – original draft, Formal analysis, Conceptualization. **Moreno Pintore:** Writing – review & editing, Formal analysis, Conceptualization. **Gioana Teora:** Writing – review & editing, Writing – original draft, Visualization, Validation, Software, Methodology, Investigation, Formal analysis, Data curation, Conceptualization. **Fabio Vicini:** Writing – review & editing, Methodology, Conceptualization.

Declaration of competing interest

The authors declare that they have no known competing financial interests or personal relationships that could have appeared to influence the work reported in this paper.

Acknowledgments

This material is based upon work supported by the Swedish Research Council under grant no. 2021-06594 while the G.T. was in residence at Institut Mittag-Leffler in Djursholm, Sweden during the Fall of 2025.

The author S.B. kindly acknowledges partial financial support provided by European Union through project Next Generation EU, M4C2, PRIN 2022 PNRR project P2022BH5CB_001 “Polyhedral Galerkin methods for engineering applications to improve disaster risk forecast and management: stabilization-free operator-preserving methods and optimal stabilization methods”, and by PNRR M4C2 project of CN00000013 National Centre for HPC, Big Data and Quantum Computing (HPC) (CUP: E13C22000990001). The author M.P. kindly acknowledges financial support provided by PEPR/IA (https://www.pepr-ia.fr/). The author G.T. kindly acknowledges the financial support provided by INdAM-GNCS Project “Metodi numerici efficienti per problemi accoppiati in sistemi complessi” (CUP: E53C24001950001). The authors L.N. and G.T. kindly acknowledge financial support provided by project NODES which has received funding from the MUR-M4C2 1.5 of PNRR funded by the European Union - NextGenerationEU (Grant agreement no. ECS00000036) and by the European Union through PRIN project 20227K44ME “Full and Reduced order modeling of coupled systems: focus on non-matching methods and automatic learning (FaReX)” (CUP: E53D23005510006). The author F.V. acknowledges the financial support by INdAM-research group GNCS, project title: “Metodi numerici avanzati per equazioni alle derivate parziali in fenomeni di trasporto e diffusione” (CUP: E53C24001950001).

Data availability

The data are available at the GitHub repository: https://github.com/AURION-Polito/Art-ZFEM-2D.

References

[1] P.G. Ciarlet, The Finite Element Method for Elliptic Problems, Society for Industrial and Applied Mathematics, 2002, http://dx.doi.org/10.1137/1.9780898719208.

[2] S.C. Brenner, L.R. Scott, The mathematical theory of finite element methods, in: Texts in Applied Mathematics, vol. 15, Springer, 2008, http://dx.doi.org/10.1007/978-0-387-75934-0.

[3] T.-P. Fries, T. Belytschko, The extended/generalized finite element method: an overview of the method and its applications, Internat. J. Numer. Methods Engrg. 84 (3) (2010) 253–304, http://dx.doi.org/10.1002/nme.2914.

[4] E. Burman, P. Hansbo, M.G. Larson, S. Zahedi, Cut finite element methods, Acta Numer. 34 (2025) 1–121, http://dx.doi.org/10.1017/S0962492925000017.

[5] T. Hughes, J. Cottrell, Y. Bazilevs, Isogeometric analysis: CAD, finite elements, NURBS, exact geometry and mesh refinement, Comput. Methods Appl. Mech. Engrg. 194 (39) (2005) 4135–4195, http://dx.doi.org/10.1016/j.cma.2004.10.008.

[6] J. Cottrell, A. Reali, Y. Bazilevs, T. Hughes, Isogeometric analysis of structural vibrations, Comput. Methods Appl. Mech. Engrg. 195 (41) (2006) 5257–5296, http://dx.doi.org/10.1016/j.cma.2005.09.027.

[7] D. Benson, Y. Bazilevs, M. Hsu, T. Hughes, Isogeometric shell analysis: The Reissner-Mindlin shell, Comput. Methods Appl. Mech. Engrg. 199 (5) (2010) 276–289, http://dx.doi.org/10.1016/j.cma.2009.05.011.

[8] C. Song, J.P. Wolf, The scaled boundary finite-element method-alias consistent infinitesimal finite-element cell method-for elastodynamics, Comput. Methods Appl. Mech. Engrg. 147 (3–4) (1997) 329–355, http://dx.doi.org/10.1016/S0165-1250(98)80005-9.

[9] S. Natarajan, E.T. Ooi, I. Chiong, C. Song, Convergence and accuracy of displacement based finite element formulations over arbitrary polygons: Laplace interpolants, strain smoothing and scaled boundary polygon formulation, Finite Elem. Anal. Des. 85 (2014) 101–122, http://dx.doi.org/10.1016/j.finel.2014.03.006.

[10] H. Gravenkamp, A.A. Saputra, S. Duczek, High-order shape functions in the scaled boundary finite element method revisited, Arch. Comput. Methods Eng. 28 (2) (2021) 473–494, http://dx.doi.org/10.1007/s11831-019-09385-1.

[11] S. Klinkel, L. Chen, W. Dornisch, A NURBS based hybrid collocation–Galerkin method for the analysis of boundary represented solids, Comput. Methods Appl. Mech. Engrg. 284 (2015) 689–711, http://dx.doi.org/10.1016/j.cma.2014.10.029.

[12] S. Rajendran, K.M. Liew, A novel unsymmetric 8-node plane element immune to mesh distortion under a quadratic displacement field, Internat. J. Numer. Methods Engrg. 58 (11) (2003) 1713–1748, http://dx.doi.org/10.1002/nme.836.

[13] E. Tat Ooi, S. Rajendran, J. Hock Yeo, Extension of unsymmetric finite elements US-QUAD8 and US-HEXA20 for geometric nonlinear analyses, Eng. Comput. 24 (4) (2007) 407–431, http://dx.doi.org/10.1108/02644400710748715.

[14] S. Eisenträger, E. Woschke, E. Ooi, Unsymmetric serendipity finite elements: Performance analysis, Finite Elem. Anal. Des. 254 (2026) 104487, http://dx.doi.org/10.1016/j.finel.2025.104487.

[15] D.A. Di Pietro, A. Ern, Mathematical Aspects of Discontinuous Galerkin Methods, vol. 69, Springer Science & Business Media, 2011, http://dx.doi.org/10.1007/978-3-642-22980-0.

[16] P.F. Antonietti, S. Bonetti, M. Botti, M. Corti, I. Fumagalli, I. Mazzieri, lymph: Discontinuous polytopal methods for multi-physics differential problems, ACM Trans. Math. Software 51 (1) (2025) http://dx.doi.org/10.1145/3716310.

[17] D.A. Di Pietro, A. Ern, A hybrid high-order locking-free method for linear elasticity on general meshes, Comput. Methods Appl. Mech. Engrg. 283 (2015) 1–21, http://dx.doi.org/10.1016/j.cma.2014.09.009.

[18] L. Beirão da Veiga, F. Brezzi, A. Cangiani, G. Manzini, A. Russo, Basic principles of virtual element methods, Math. Models Methods Appl. Sci. 23 (01) (2013) 199–214, http://dx.doi.org/10.1142/S0218202512500492.

[19] L. Beirão da Veiga, F. Brezzi, L. Marini, A. Russo, The hitchhiker's guide to the virtual element method, Math. Models Methods Appl. Sci. 24 (08) (2014) 1541–1573, http://dx.doi.org/10.1142/S021820251440003X.

[20] E.L. Wachspress, A rational finite element basis, A Rational Finite Element Basis, vol. 114, Academic Press, New York, 1975.

[21] N. Sukumar, A. Tabarraei, Conforming polygonal finite elements, Internat. J. Numer. Methods Engrg. 61 (12) (2004) 2045–2066, http://dx.doi.org/10.1002/nme.1141.

[22] M.S. Floater, Mean value coordinates, Comput. Aided Geom. Design 20 (1) (2003) 19–27, http://dx.doi.org/10.1016/S0167-8396(03)00002-5.

[23] M.S. Floater, G. Kós, M. Reimers, Mean value coordinates in 3D, Comput. Aided Geom. Design 22 (7) (2005) 623–631, http://dx.doi.org/10.1016/j.cagd.2005.06.004, Geometric Modelling and Differential Geometry.

[24] N. Sukumar, Construction of polygonal interpolants: a maximum entropy approach, Internat. J. Numer. Methods Engrg. 61 (12) (2004) 2159–2181, http://dx.doi.org/10.1002/nme.1193.

[25] N. Sukumar, B. Moran, T. Belytschko, The natural element method in solid mechanics, Internat. J. Numer. Methods Engrg. 43 (5) (1998) 839–887, http://dx.doi.org/10.1002/(SICI)1097-0207(19981115)43:5<839::AID-NME423>3.0.CO;2-R.

[26] N. Sukumar, B. Moran, A. Yu Semenov, V.V. Belikov, Natural neighbour Galerkin methods, Internat. J. Numer. Methods Engrg. 50 (1) (2001) 1–27, http://dx.doi.org/10.1002/1097-0207(20010110)50:1<1::AID-NME14>3.0.CO;2-P.

[27] C. Talischi, G.H. Paulino, A. Pereira, I.F. Menezes, Polygonal finite elements for topology optimization: A unifying paradigm, Internat. J. Numer. Methods Engrg. 82 (6) (2010) 671–698, http://dx.doi.org/10.1002/nme.2763.

[28] E.A. Malsch, G. Dasgupta, Shape functions for polygonal domains with interior nodes, Internat. J. Numer. Methods Engrg. 61 (8) (2004) 1153–1172, http://dx.doi.org/10.1002/nme.1099.

[29] G.R. Liu, K.Y. Dai, T.T. Nguyen, A smoothed finite element method for mechanics problems, Comput. Mech. 39 (6) (2007) 859–877, http://dx.doi.org/10.1007/s00466-006-0075-4.

[30] K.-Y. Dai, G.-R. Liu, T.-T. Nguyen, An n-sided polygonal smoothed finite element method (nSFEM) for solid mechanics, Finite Elem. Anal. Des. 43 (11–12) (2007) 847–860, http://dx.doi.org/10.1016/j.finel.2007.05.009.

[31] W. Zeng, G.R. Liu, Smoothed finite element methods (S-FEM): an overview and recent developments, Arch. Comput. Methods Eng. 25 (2) (2018) 397–435, http://dx.doi.org/10.1007/s11831-016-9202-3.

[32] M. Trezzi, U. Zerbinati, When rational functions meet virtual elements: the lightning virtual element method, Calcolo 61 (3) (2024) 35, http://dx.doi.org/10.1007/s10092-024-00585-1.

[33] F. Credali, S. Bertoluzza, D. Prada, Reduced basis stabilization and post-processing for the virtual element method, Comput. Methods Appl. Mech. Engrg. 420 (2024) 116693, http://dx.doi.org/10.1016/j.cma.2023.116693.

[34] S. Berrone, M. Pintore, G. Teora, The lowest-order neural approximated virtual element method on polygonal elements, Comput. Struct. 314 (2025) 107753, http://dx.doi.org/10.1016/j.compstruc.2025.107753.

[35] S. Berrone, M. Pintore, G. Teora, The neural approximated virtual element method for elasticity problems, Finite Elem. Anal. Des. 252 (2025) 104467, http://dx.doi.org/10.1016/j.finel.2025.104467.

[36] S. Duczek, U. Gabbert, The finite cell method for polygonal meshes: poly-FCM, Comput. Mech. 58 (2016) 587–618, http://dx.doi.org/10.1007/s00466-016-1307-x.

[37] G. Karniadakis, S. Sherwin, Spectral/hp Element Methods for Computational Fluid Dynamics, Oxford University Press, 2005, http://dx.doi.org/10.1093/acprof:oso/9780198528692.001.0001.

[38] H. Xu, C.D. Cantwell, C. Monteserin, C. Eskilsson, A.P. Engsig-Karup, S.J. Sherwin, Spectral/hp element methods: Recent developments, applications, and perspectives, J. Hydrodyn. 30 (1) (2018) 1–22, http://dx.doi.org/10.1007/s42241-018-0001-1.

[39] T. Arbogast, Z. Tao, C. Wang, Direct Serendipity and mixed finite elements on convex quadrilaterals, Numer. Math. 150 (4) (2022) 929–974, http://dx.doi.org/10.1007/s00211-022-01274-3.

[40] T. Arbogast, C. Wang, Direct Serendipity and mixed finite elements on convex polygons, Numer. Algorithms 92 (2) (2023) 1451–1483, http://dx.doi.org/10.1007/s11075-022-01348-1.

[41] S. Duczek, A. Saputra, H. Gravenkamp, High order transition elements: The xNy-element concept - Part I: Statics, Comput. Methods Appl. Mech. Engrg. 362 (2020) 112833, http://dx.doi.org/10.1016/j.cma.2020.112833.

[42] S. Eisenträger, J. Eisenträger, H. Gravenkamp, C. Provatidis, High order transition elements: The xNy-element concept, Part II: Dynamics, Comput. Methods Appl. Mech. Engrg. 387 (2021) 114145, http://dx.doi.org/10.1016/j.cma.2021.114145.

[43] C. Provatidis, S. Eisenträger, Macroelement analysis in T-patches using Lagrange polynomials, Mathematics 13 (9) (2025) 1498, http://dx.doi.org/10.3390/math13091498.

[44] C.G. Provatidis, R. Sevilla, D. Schillinger, S. Eisenträger, Revisiting Transfinite Elements: Unifying Element Formulations for IGA, SEM, NEFEM, p-FEM and h-FEM, Arch. Comput. Methods Eng. (2025) http://dx.doi.org/10.1007/s11831-025-10351-3.

[45] E.L. Wachspress, High-order curved finite elements, Internat. J. Numer. Methods Engrg. 17 (5) (1981) 735–745, http://dx.doi.org/10.1002/nme.1620170507.

[46] P. Milbradt, T. Pick, Polytope finite elements, Internat. J. Numer. Methods Engrg. 73 (12) (2008) 1811–1835, http://dx.doi.org/10.1002/nme.2149.

[47] S. Berrone, M. Pintore, G. Teora, Two continuous extensions of neural approximated virtual element methods, 2026, http://dx.doi.org/10.48550/arXiv.2601.09595, arXiv:2601.09595.

[48] J. Bishop, A displacement-based finite element formulation for general polyhedra using harmonic shape functions, Internat. J. Numer. Methods Engrg. 97 (1) (2014) 1–31, http://dx.doi.org/10.1002/nme.4562.
[49] A. Bunge, P. Herholz, M. Kazhdan, M. Botsch, Polygon Laplacian made simple, Comput. Graph. Forum 39 (2) (2020) 303–313, http://dx.doi.org/10.1111/cgf.13931.
[50] A. Bunge, P. Herholz, O. Sorkine-Hornung, M. Botsch, M. Kazhdan, Variational quadratic shape functions for polygons and polyhedra, ACM Trans. Graph. 41 (4) (2022) http://dx.doi.org/10.1145/3528223.3530137.
[51] S. Berrone, A. Borio, G. Teora, F. Vicini, POLYDIM: A c++ library for polytopal discretization methods, Comput. Phys. Comm. 320 (2026) 109937, http://dx.doi.org/10.1016/j.cpc.2025.109937.
[52] L.C. Evans, Partial differential equations, in: Graduate Studies in Mathematics, vol. 19, American Mathematical Society, 2010, http://dx.doi.org/10.1090/gsm/019.
[53] L. Beirão da Veiga, F. Brezzi, L. Marini, A. Russo, Serendipity Nodal VEM spaces, Comput. & Fluids 141 (2016) 2–12, http://dx.doi.org/10.1016/j.compfluid.2016.02.015.
[54] G.C. Calafiore, L. El Ghaoui, Optimization Models, Cambridge University Press, 2014, http://dx.doi.org/10.1017/CBO9781107279667.
[55] S.C. Brenner, Q. Guan, L.-Y. Sung, Some estimates for virtual element methods, Comput. Methods Appl. Math. 17 (4) (2017) 553–574, http://dx.doi.org/10.1515/cmam-2017-0008.
[56] G.E. Fasshauer, Meshfree Approximation Methods with Matlab, World Scientific, 2007, http://dx.doi.org/10.1142/6437.
[57] N.J. Higham, Cholesky factorization, Wiley Interdiscip. Rev.: Comput. Stat. 1 (2) (2009) 251–254, http://dx.doi.org/10.1002/wics.18.
[58] L. Beirão da Veiga, F. Brezzi, L.D. Marini, A. Russo, Virtual element method for general second order elliptic problems on polygonal meshes, Math. Models Methods Appl. Sci. 26 (04) (2016) 729–750, http://dx.doi.org/10.1142/S0218202516500160.
[59] S. Berrone, A. Borio, G. Teora, F. Vicini, GeDiM: Geometry for discretization method library, 2025, http://dx.doi.org/10.5281/zenodo.15146658.
[60] C.H. Rycroft, VORO++: A three-dimensional Voronoi cell library in C++, Chaos: An Interdiscip. J. Nonlinear Sci. 19 (4) (2009) 041111, http://dx.doi.org/10.1063/1.3215722.
[61] J.R. Shewchuk, Triangle: Engineering a 2D quality mesh generator and delaunay triangulator, in: M.C. Lin, D. Manocha (Eds.), Applied Computational Geometry: Towards Geometric Engineering, in: Lecture Notes in Computer Science, vol. 1148, Springer-Verlag, 1996, pp. 203–222, http://dx.doi.org/10.1007/BFb0014497, From the First ACM Workshop on Applied Computational Geometry.
[62] A. Fumagalli, E. Keilegavlen, S. Scialò, Conforming, non-conforming and non-matching discretization couplings in discrete fracture network simulations, J. Comput. Phys. 376 (2019) 694–712, http://dx.doi.org/10.1016/j.jcp.2018.09.048.
[63] M.F. Benedetto, S. Berrone, S. Scialò, A globally conforming method for solving flow in discrete fracture networks using the Virtual Element Method, Finite Elem. Anal. Des. 109 (2016) 23–36, http://dx.doi.org/10.1016/j.finel.2015.10.003.
[64] S. Berrone, F. Vicini, Effective polygonal mesh generation and refinement for VEM, Math. Comput. Simulation 231 (2025) 239–258, http://dx.doi.org/10.1016/j.matcom.2024.12.007.